Valence QCD: Connecting QCD to the quark model

K. F. Liu,[1] S. J. Dong,[1] T. Draper,[1] D. Leinweber,[2] J. Sloan,[1] W. Wilcox,[3] and R. M. Woloshyn[4]
[1]*Department of Physics and Astronomy, University of Kentucky, Lexington, Kentucky 40506*
[2]*Special Research Centre for the Subatomic Structure of Matter and Department of Physics and Mathematical Physics, University of Adelaide, Adelaide, Australia 5005*
[3]*Department of Physics, Baylor University, Waco, Texas 76798*
[4]*TRIUMF, 4004 Wesbrook Mall, Vancouver, British Columbia, Canada V6T 2A3*
(Received 26 June 1998; revised manuscript 3 December 1998; published 27 April 1999)

A valence QCD theory is developed to study the valence quark properties of hadrons. To keep only the valence degrees of freedom, the pair creation through the Z graphs is deleted in the connected insertions, whereas the sea quarks are eliminated in the disconnected insertions. This is achieved with a new ''valence QCD'' Lagrangian where the action in the time direction is modified so that the particle and antiparticle decouple. It is shown in this valence version of QCD that the ratios of isovector to isoscalar matrix elements (e.g., F_A/D_A and F_S/D_S ratios) in the nucleon reproduce the SU(6) quark model predictions in a lattice QCD calculation. We also consider how the hadron masses are affected on the lattice and discover new insights into the origin of dynamical mass generation. It is found that, within statistical errors, the nucleon and the Δ become degenerate for the quark masses we have studied (ranging from 1 to 4 times the strange mass). The π and ρ become nearly degenerate in this range. It is shown that valence QCD has the C, P, T symmetries. The lattice version is reflection positive. It also has the vector and axial symmetries. The latter leads to a modified partially conserved axial Ward identity. As a result, the theory has a $U(2N_F)$ symmetry in the particle-antiparticle space. Through lattice simulation, it appears that this is dynamically broken down to $U_q(N_F)\times U_{\bar{q}}(N_F)$. Furthermore, the lattice simulation reveals spin degeneracy in the hadron masses and various matrix elements. This leads to an approximate $U_q(2N_F)\times U_{\bar{q}}(2N_F)$ symmetry which is the basis for the valence quark model. In addition, we find that the masses of N, Δ,ρ,π,a_1, and a_0 all drop precipitously compared to their counterparts in the quenched QCD calculation. This is interpreted as due to the disappearance of the ''constituent'' quark mass which is dynamically generated through tadpole diagrams. The origin of the hyperfine splitting in the baryon is largely attributed to the Goldstone boson exchanges between the quarks. Both of these are the consequences of the lack of chiral symmetry in valence QCD. We discuss its implications concerning the models of hadrons. [S0556-2821(99)01009-7]

PACS number(s): 12.38.Gc, 11.30.Rd, 12.39.Ki

I. INTRODUCTION

In addition to its classification scheme, the quark model is, by and large, quite successful in delineating the spectrum, structure, and decays of mesons and baryons. One often wonders what the nature of the approximation is, especially in view of the advent of quantum chromodynamics (QCD), which is believed to be, after all, the fundamental theory of quarks and gluons. In order to address this question, we need to understand first where the quark model is successful and where it fails.

To begin with, we need to define what we mean by the quark model. We consider the simplest approach which includes the following ingredients.

(i) The Fock space is restricted to the valence quarks only, i.e. three quarks for the baryon and a quark-antiquark pair for the meson. Although there are variations which include quark self-energy and so on which go beyond the instantaneous interaction and invoke higher Fock space (e.g., $q^4\bar{q}$ for the baryon and $q^2\bar{q}^2$ for the meson), we will not consider them here.

(ii) These valence quarks, be they dressed constituent quarks or bare quarks, are confined to a potential or a bag. To this zeroth order, the hadron wave functions involving u, d, and s quarks and antiquarks are classified by the flavor-spin and spatial coordinates according to the $SU_q(6)\times SU_{\bar{q}}(6)\times O(3)$ group [for brevity, we shall refer to it as SU(6)]. The wave functions are totally antisymmetric in the color space for the baryons and symmetric in the color-anticolor combinations for the mesons. For example, the S- and D-wave baryons are described by the 56-plets and the P-wave baryons by the 70-plets. Similarly, the S- and P-wave mesons are described by the 36-plets [1].

(iii) The SU(6) symmetry is broken down to $SU(3)\times SU(2)$ by the residual interaction between the quarks which is weak compared to the confining potential. The degeneracies within the multiplets are lifted by these residual interactions. Of course, additional breakings of flavor SU(3) due to the quark masses are responsible for the detailed splitting within the octet-decuplet baryon multiplets and the meson nonets.

There are many different versions of the quark model which share these attributes. They have been called the naive quark model, nonrelativistic quark model, constituent quark model, bag model, etc., in the literature. Here we shall refer to them generically as the valence quark model with the defining features of the lowest Fock space (or valence Fock space) and the SU(6) flavor-spin symmetry, albeit approximate, as their common denominator. In this work, we shall

concentrate our discussion on the light quark systems where the valence quark picture is less well understood. For mesons with heavy quarks, such as charmoniums and upsilons, the valence picture based on the nonrelativistic potential model which fits experiments reasonably well is confirmed by the nonrelativistic lattice QCD calculations [2–5]. We shall not address them in this study.

Given the definition of the valence quark model, it is as easy to understand where it succeeds as where it fails. For example, with the one-gluon-like exchange potential [6] as the residual interaction between the nonrelativistically confined quarks describing the hyperfine and fine splittings of the hadron masses, the valence quark model is very successful in fitting meson and baryon masses [7–10] and baryon magnetic moments [6,11,12]. It is also successful in delineating the pattern of electromagnetic (EM) [1,13,14], semileptonic and nonleptonic weak decays [15], the Okubo-Zweig-Iizuka (OZI) rule [16], etc. Similarly it is true for the MIT bag model where the relativistic quarks and antiquarks are confined in a bag with a one-gluon-exchange interaction [17,18].

It is worthwhile noting that all these are based on the valence quark picture augmented by the $SU(6)\times O(3)$ for its flavor-spin and space group. On the other hand, there are notable failures. For example, it fails to account for the U(1) anomaly (the η' mass), the proton spin crisis, and the $\pi N\sigma$ term. All these problems are associated with large contributions from disconnected insertions involving sea quarks [19–21]. These are places where the OZI rule fails badly. Consequently, it is natural not to expect the valence quark model to work in these cases.

There are also other places where the valence quark model does not work well. They include hadron scatterings, couplings, and form factors which are well described by models utilizing the chiral symmetry inherent in QCD. Examples of successful approaches based on chiral symmetry include $\pi\pi$ scattering [22,23], vector dominance [24], the Kawarabayashi-Suzuki-Riazuddin-Fayyazuddin (KSRF) relation [25], low-energy πN scatterings [22,26], πN scattering up to about 1 GeV with the Skyrmion [27], nucleon static properties [28], electromagnetic form factors [28], πNN form factor [29], NN interaction, and Goldberger-Treiman relation [30]. All these have been worked out quite successfully by parallel developments which explore the chiral symmetry of QCD. These include the σ model, current algebra, PCAC (partial conservation of axial vector current), chiral perturbation theory, and the more recent developments incorporating large N_c QCD [31,32], such as the Skyrmion [28,33] and the contracted current algebra [34].

The common theme of these models is chiral symmetry which involves the meson cloud in the baryon and thus the higher Fock space beyond the valence. This cloud degree of freedom is essential in the case of the vector dominance of EM form factors, the pion cloud for the Goldberger-Treiman relation, and the nonvanishing neutron electric form factor. Therefore, it is a challenge to understand why the valence quark model ''works'' without spontaneously broken chiral symmetry and where the hyperfine splitting in hadron spectroscopy and the constitute quark mass come from.

From the above discussion, it is clear that the Fock space beyond the valence is important and we mentioned two degrees of freedom, namely, cloud and sea. How to relate these degrees of freedom back to QCD unambiguously, how to find out their roles in physical quantities, and, more importantly, how to relate them to chiral symmetry are the main subjects of this paper. It turns out that chiral symmetry plays essential roles in light hadron spectroscopy as well as hadron structure. We find that both the ''constituent'' quark mass and the hyperfine splitting in light baryons are more of a consequence of spontaneous chiral symmetry breaking than that of gluons and sea quarks.

In Sec. II, we will define these dynamical degrees of freedom in the Euclidean path integral formalism for the hadronic tensor in deep inelastic scattering. In Sec. III, we introduce a valence QCD theory which modifies QCD to eliminate quark-antiquark pair production, thus suppressing both the cloud and sea degrees of freedom. The discrete and continuous symmetries of valence QCD are explored. In Sec. IV, we adopt a lattice action for valence QCD and prove its reflection positivity and Hermiticity. The pion mass, the pion decay constant, and the current quark mass from the axial Ward identity are used to define the zero-quark-mass limit on the lattice. In Sec. V, we calculate various ratios of matrix elements to check the SU(6) relations. The nucleon form factors are calculated and presented in Sec. VI. We then study hadron spectroscopy in comparison with that of QCD to explore the origin of the hyperfine splitting and the ''constituent'' quark mass in Sec. VII. Perhaps the most exciting aspect of valence QCD is a new understanding of the origin of dynamical mass generation, something missing in the valence quark model and put in by hand via a constituent quark mass. In Sec. VIII, we compare the symmetry breaking patterns in valence QCD and QCD. Finally, in Sec. IX, we summarize the lessons learned from the valence QCD and draw an analogy between the valence quark model and the nuclear shell model. We will also discuss the implication for model building of hadrons.

II. QUARK DYNAMICAL DEGREES OF FREEDOM

We have so far alluded to the meson clouds and sea quarks in addition to the valence quarks. They appear in various QCD-inspired hadronic models and effective theories. How does one define the valence, the cloud, and the sea quarks unambiguously and in a model-independent way in QCD? It turns out that the best way of revealing these dynamical degrees of freedom is in deep inelastic scattering where the quarks show up as the parton densities.

The deep inelastic scattering of a muon on a nucleon involves the hadronic tensor which, being an inclusive reaction, involves all intermediate states:

$$W_{\mu\nu}(q^2,\nu)=\frac{1}{2M_N}\sum_n (2\pi)^3\delta^4(p_n-p-q) \times\langle N|J_\mu(0)|n\rangle\langle n|J_\nu(0)|N\rangle_{spin\ ave}. \quad (1)$$

Since deep inelastic scattering measures the absorptive part of the Compton scattering, it is the imaginary part of the

forward amplitude and can be expressed as the current-current correlation function in the nucleon, i.e.,

$$W_{\mu\nu}(q^2,\nu)=\frac{1}{\pi}\mathrm{Im}\,T_{\mu\nu}(q^2,\nu)$$
$$=\frac{1}{2M_N}\left\langle N\left|\int\frac{d^4x}{2\pi}e^{iq\cdot x}J_\mu(x)J_\nu(0)\right|N\right\rangle_{spin\ ave}. \tag{2}$$

It has been shown [35] that the hadronic tensor $W_{\mu\nu}(q^2,\nu)$ can be obtained from the Euclidean path-integral formalism where the various quark dynamical degrees of freedom are readily and explicitly revealed (Fig. 1). In this case, one considers the ratio of the four-point function $\langle O_N(t)J_\nu(\vec{x},t_2)J_\mu(0,t_1)O_N(0)\rangle$ and the two-point function $\langle O_N(t-(t_2-t_1))O_N(0)\rangle$, where $O_N(t)$ is an interpolation field for the nucleon with momentum p at Euclidean time t.

As both $t-t_2\gg 1/\Delta M_N$ and $t_1\gg 1/\Delta M_N$, where ΔM_N is the mass gap between the nucleon and the next excitation (i.e., the threshold of a nucleon and a pion in the p wave), the contributions generated by the interpolation field O_N will be dominated by the nucleon with the Euclidean propagator $e^{-M_N[(t-t_2)+t_1]}$. Hence,

$$\tilde{W}_{\mu\nu}(\vec{q}^{\,2},\tau)=\left.\frac{(1/2M_N)\left\langle O(t)\int(d^3x/2\pi)e^{-i\vec{q}\cdot\vec{x}}J_\mu(\vec{x},t_2)J_\nu(0,t_1)O(0)\right\rangle}{\langle O(t-\tau)O(0)\rangle}\right|_{\substack{t-t_2\gg 1/\Delta M_N\\ t_1\gg 1/\Delta M_N}}$$
$$=\frac{(f^2/2M_N)e^{-M_N(t-t_2)}\langle N|\int(d^3x/2\pi)\,e^{-i\vec{q}\cdot\vec{x}}J_\mu(\vec{x},t_2)J_\nu(0,t_1)|N\rangle e^{-M_Nt_1}}{f^2e^{-M_N(t-\tau)}}$$
$$=\frac{1}{2M_NV}\langle N|\int\frac{d^3x}{2\pi}e^{-i\vec{q}\cdot\vec{x}}J_\mu(\vec{x},t_2)J_\nu(0,t_1)|N\rangle, \tag{3}$$

where $\tau=t_2-t_1$, f is the transition matrix element $\langle 0|O_N|N\rangle$, and V is the three-volume. Inserting intermediate states, $\tilde{W}_{\mu\nu}(\vec{q}^{\,2},\tau)$ becomes

$$\tilde{W}_{\mu\nu}(\vec{q}^{\,2},\tau)=\frac{1}{2M_NV}\sum_n(2\pi)^2\delta^3(p_n-p+q)\langle N|J_\mu(0)|n\rangle$$
$$\times\langle n|J_\nu(0)|N\rangle_{spin\ ave}e^{-(E_n-E_N)\tau}. \tag{4}$$

We see from Eq. (4) that the time dependence is in the exponential factor $e^{-(E_n-E_N)\tau}$. To go back to the delta function $\delta(E_n-E_N+\nu)$ in Eq. (1), one needs to carry out the inverse Laplace transform [36,35]

$$W_{\mu\nu}(q^2,\nu)=\frac{V}{i}\int_{c-i\infty}^{c+i\infty}d\tau e^{\nu\tau}\tilde{W}_{\mu\nu}(\vec{q}^{\,2},\tau). \tag{5}$$

This is basically doing an anti-Wick rotation back to Minkowski space.

In the Euclidean path-integral formulation of $\tilde{W}_{\mu\nu}(\vec{q}^{\,2},\tau)$, contributions to the four-point function can be classified according to different topologies of the quark paths between the source and the sink of the proton. They represent different ways the fields in the currents J_μ and J_ν contract with those in the nucleon interpolation operator O_N. This is so because the quark action and the electromagnetic currents are both bilinear in quark fields, i.e., of the form $\bar{\Psi}M\Psi$, so that the quark number is conserved and as a result the quark line does not branch the way a gluon line does. Figures 1(a) and 1(b) represent connected insertions (CIs) of the currents. Figure 1(c), on the other hand, represents a disconnected insertion (DI) where the quark fields from J_μ and J_ν self-contract and are hence disconnected from the quark paths between the proton source and sink. Here, ''disconnected'' refers only to the quark lines. Of course, quarks swim in the background of the gauge field and all quark paths are ultimately connected through the gluon lines.

The infinitely many possible gluon lines and additional quark loops are implicitly there in Fig. 1 but are not explicitly drawn. Figure 1 represents the contributions of the class of ''handbag'' diagrams where the two currents are hooked on the same quark line. These include leading twist contributions in deep inelastic scattering.

The other contractions involving the two currents hooking onto different quark lines are represented in Fig. 2. Given a renormalization scale, these are higher-twist contributions in

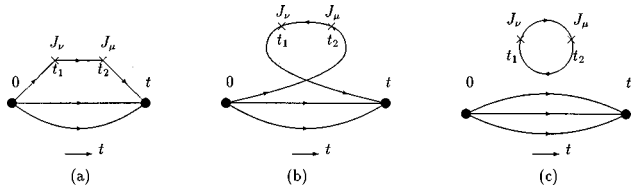

FIG. 1. Quark skeleton diagrams in Euclidean path-integral formalism for evaluating $W_{\mu\nu}$ from the four-point function defined in Eq. (3). These include the lowest-twist contributions to $W_{\mu\nu}$. (a) and (b) are the connected insertions and (c) is the disconnected insertion.

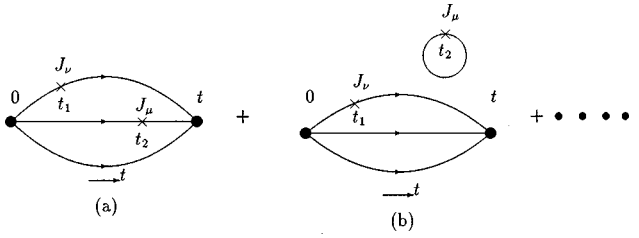

FIG. 2. Quark skeleton diagrams similar to those in Fig. 1, except that the two current insertions are on different quark lines. These correspond to higher-twist contributions to $W_{\mu\nu}$ and are suppressed by $1/Q^2$.

the Bjorken limit. Details of the operator product expansion will be given elsewhere [37]. From now on, we will neglect these ''cat's ears'' diagrams in Fig. 2.

In the deep inelastic limit where $x^2 \leqslant O(1/Q^2)$ (we are using the Minkowski notation here), the leading light-cone singularity of the current product (or commutator) gives rise to a free quark propagator between the currents. In the time-ordered diagrams in Fig. 1, Fig. 1(a) [Fig. 1(b)] involves only a quark [antiquark] propagator between the currents, whereas Fig. 1(c) has both quark and antiquark propagators. Hence, there are two distinct classes of diagrams where the antiquarks contribute. One comes from the DI; the other comes from the CI. It is frequently assumed that connected insertions involve only ''valence'' quarks which are responsible for the baryon number. This is not true. To define the quark distribution functions more precisely, we shall call the antiquark distribution from the DI (which is connected to the ''valence'' quark propagators and other quark loops through gluons) the ''sea'' quark. We shall refer to the antiquark in the backward-time-going quark propagator between t_1 and t_2 in Fig. 1(b) as the ''cloud'' antiquark. On the other hand, the quark in the time-forward propagator between t_2 and t_1 in Fig. 1(a) includes both the valence and the cloud quarks. This is because a quark propagator from $t=0$ to $t=t$ $(t>0)$ involves both time-forward and -backward zigzag motions so that one cannot tell if the quark propagator between t_2 and t_1 is due to the valence or the cloud. All one knows is that it is a quark propagator. In other words, one needs to consider cloud quarks in addition to the valence to account for the production of cloud quark-antiquark pairs in a connected fashion [Fig. 1(a)], whereas the pair production in a disconnected fashion is in Fig. 1(c).

One important point to raise at this stage is that this separation into valence, anticloud, and sea is gauge invariant [i.e., in the path-integral formalism of Eq. (4), no gauge fixing is required] and topologically distinct as far as the quark skeleton diagrams in Fig. 1 are concerned. However, the separation depends on the frame of the nucleon. It is expected that the parton model acquires its natural interpretation in the large momentum frame of the nucleon, i.e., $p \geqslant q$. Consequently, in the large momentum frame, the parton density for the u and d antiquarks comes from two sources:

$$\bar{q}(x) = \bar{q}_c(x) + \bar{q}_s(x), \tag{6}$$

where $\bar{q}_c(x)$ is the cloud antiparton distribution from the CI in Fig. 1(b) and $\bar{q}_s(x)$ denotes the sea antiparton distribution from the DI in Fig. 1(c). The strange and charm quarks would only contribute in the DI in Fig. 1(c). Similarly, the u and d quarks have two sources, i.e.,

$$q(x) = q_{V+c}(x) + q_s(x), \tag{7}$$

where $q_{V+c}(x)$, denoting the valence and cloud quarks, and $q_s(x)$, denoting the sea quark, are from Fig. 1(a) and Fig. 1(c), respectively. Upon defining $q_c(x) = \bar{q}_c(x)$ (note that the subscript c denotes the cloud not charm), the valence parton distribution is obtained by

$$q_V(x) = q_{V+c}(x) - \bar{q}_c(x), \tag{8}$$

and is responsible for the baryon number, i.e., $\int u_V(x)dx = \int [u(x) - \bar{u}(x)]dx = 2$ and $\int d_V(x)dx = \int [d(x) - \bar{d}(x)] = 1$ for the proton.

It has been shown [35] that the sea partons in Fig. 1(c) cannot give rise to a large Gottfried sum rule violation, i.e., $\bar{u}_s(x) = \bar{d}_s(x)$, instead the origin of $\bar{u}(x) \neq \bar{d}(x)$ comes primarily from the cloud antipartons in Fig. 1(b).

After the dynamical degrees of freedom are established in deep inelastic scattering (DIS), we need to address their relevance to the quark model. The quark model is designed to delineate hadron properties in the rest frame or at low energies, such as hadron masses, decay constants, form factors, electroweak transitions, etc. Unlike the hadronic tensor which entails the calculation of four-point functions as illustrated in Eq. (4), these quantities involve two-point and three-point functions. The question is, where do the dynamical degrees of freedom reside in the three-point functions which describe the matrix elements of hadrons? To track the degrees of freedom, we can consider the operator product expansion as an illustration.

Since the momentum transfer $|\vec{q}|$ and energy transfer ν are large in DIS, the product of currents in the forward Compton amplitude $T_{\mu\nu}(q^2, \nu)$ can be expanded as a series of local operators. The matrix elements of these local quark bilinear operators are then related to the moments of the parton distribution. The details will be given elsewhere [37]. We simply note that the effect of expanding in terms of $1/Q^2$ pinches the separation of the two currents (i.e., t_1 and t_2 in Fig. 1) into one space-time point. Thus the topologically distinct contributions to the four-point functions extracted from Figs. 1(a), 1(b), and 1(c) are related to the matrix elements obtainable from the three-point functions in Figs. 3(a), 3(b), and 3(c), respectively. The latter represents matrix elements of the series of the local operators. Notice that for any single matrix element related to the quark bilinear operator $\bar{\Psi}\Gamma\Psi$, i.e., $\langle N|\bar{\Psi}\Gamma\Psi|N\rangle$, Fig. 3(c), which inherits the sea degree of freedom from Fig. 1(c), is still distinct from Fig. 3(a) and 3(b) and continues to be a DI. On the other hand, Figs. 3(a) and 3(b) are no longer topologically distinct. In fact, they represent the *same* CI for the local operator. Therefore, the valence and cloud degrees of freedom from Figs. 1(a) and 1(b) are lumped together in the CI of three-point functions.

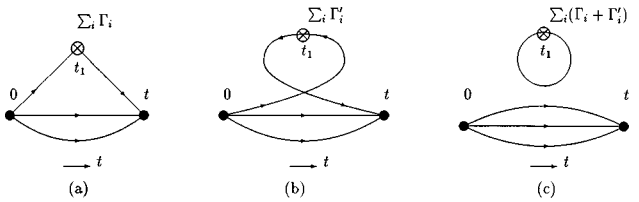

FIG. 3. Quark skeleton diagrams in the Euclidean path-integral formalism considered in the evaluation of matrix elements for the sum of local operators from the operator product expansion of $J_\mu(x)J_\nu(0)$. (a), (b), and (c) corresponds to the operator product expansion from Figs. 1(a), 1(b), and 1(c), respectively.

They cannot be separated in a single matrix element in contrast to the case for four-point functions.

What we have shown in this section is that for a flavor-singlet current $\bar{\Psi}\Gamma\Psi$, the matrix element $\langle N|\bar{\Psi}\Gamma\Psi|N\rangle$ has both the CI [Figs. 3(a) and 3(b) represent the same CI in this case] and the DI [Fig. 3(c)]. While one can study the sea effect directly from the DI, one cannot separately study the valence and the cloud in the Z graphs since both are included in the CI and Figs. 3(a) and 3(b) are topologically indistinguishable. Similarly one can trace the quark degrees of freedom in decay constants and hadron masses which are obtainable from the two-point functions. The flavor-nonsinglet hadrons are obtainable from the CI depicted in Fig. 4(a). The flavor-singlet meson, e.g., η', also involves the DI in Fig. 4(b). The quark propagators in the two-point functions in Figs. 4(a) and 4(b) include the valence and cloud (Z graphs) only; they do not involve the sea contribution. The sea effects come only through the fermion determinant in this case.

III. VALENCE QCD

After having examined the roles of the quark dynamical degrees of freedom, we come back to the question of what approximation to QCD the valence quark model represents. As illustrated in Fig. 3, the sea is only involved in the DI part of the three-point function and thus can be isolated. On the other hand, as stressed in Sec. II, the cloud and valence contributions are lumped in the CI in Fig. 3 [Figs. 3(a) and 3(b) are the same for a single quark bilinear operator $\bar{\Psi}\Gamma\Psi$] and cannot be separated *a posteriori*. Thus to single out the valence effects requires an approximation to QCD. This can be achieved by forcibly eliminating pair creation and annihilation by decoupling the quark from the antiquark. In other words, we want to eliminate all Z graphs such as the typical one illustrated in Fig. 5. We introduce valence QCD (VQCD), a theory which is designed to achieve this goal.

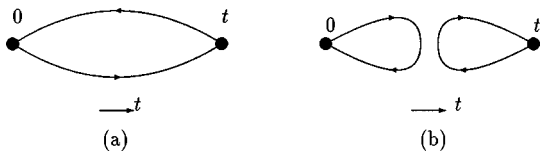

FIG. 4. (a) The connected insertion for a meson propagator. (b) The disconnected insertion part for the flavor-singlet meson propagator which involves the annihilation channel.

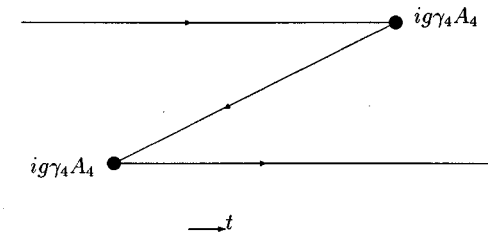

FIG. 5. A typical Z graph as a diagram in time-ordered perturbation.

First of all, we shall introduce the particle field u and the antiparticle field v in lieu of the Dirac field Ψ in the valence QCD Lagrangian

$$\mathcal{L}_{VQCD} = -\frac{1}{4}F_{\mu\nu}F_{\mu\nu} - \bar{u}\left[\frac{\gamma_4+1}{2}D_4 + \vec{\gamma}\cdot\vec{D} + m\right]u - \bar{v}\left[\frac{\gamma_4-1}{2}D_4 + \vec{\gamma}\cdot\vec{D} + m\right]v. \quad (9)$$

Comparing with the QCD Lagrangian, the valence version has changed the γ_4 into $(\gamma_4+1)/2$ for the particle field u and $(\gamma_4-1)/2$ for the antiparticle field v. We note that the u and v fields do not couple. Now we want to prove that the propagator of the u field only propagates forward in time and does not zigzag in the time direction to generate particle-antiparticle pairs. The propagator $S_u(x,y;A)$ satisfies the equation

$$-\left(\frac{\gamma_4+1}{2}D_4 + \vec{\gamma}\cdot\vec{D} + m\right)S_u(x,y;A) = \delta(x-y). \quad (10)$$

This can be cast in an integral representation with the static propagator $S_u^0(x,y;A_4)$ as the bare part of the solution [38]. The static propagator $S_u^0(x,y;A_4)$ satisfies the following equation with no propagation in the spatial direction:

$$-\left(\frac{\gamma_4+1}{2}D_4 + m\right)S_u^0(x,y;A_4) = \delta(x-y). \quad (11)$$

It is easy to write down the formal solution for $S_u^0(x,y;A_4)$:

$$S_u^0(x,y;A_4) = -\theta(x_4-y_4)e^{-m(x_4-y_4)}\frac{1+\gamma_4}{2}P\begin{bmatrix}x\\y\end{bmatrix}\delta(\vec{x}-\vec{y}) - \frac{\delta(x_4-y_4)}{m}e^{-m(y_4-x_4)}\frac{1-\gamma_4}{2}P\begin{bmatrix}x\\y\end{bmatrix}\delta(\vec{x}-\vec{y}), \quad (12)$$

where

$$P\begin{bmatrix}x\\y\end{bmatrix} \equiv P\exp\left(ig\int_{y_4}^{x_4} dz_4 A_4\right)$$

is the path-ordered parallel transport factor in the time direction. We see that the usual antiparticle propagation in QCD

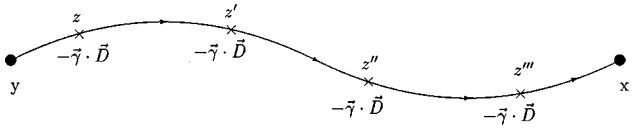

FIG. 6. A term in the hopping expansion series in Eq. (14) is graphically presented.

which involves the $\theta(y_4-x_4)$ is now replaced by $\delta(x_4-y_4)$ in the second term. Thus, $S_u^0(x,y;A_4)$ is the static particle propagator which moves forward in time only. Now the full propagator $S_u(x,y;A)$ can be represented in an integral equation in terms of $S_u^0(x,y;A_4)$:

$$S_u(x,y;A)=S_u^0(x,y;A_4)+\int d^4z S_u^0(x,z;A_4)\vec{\gamma}\cdot\vec{D}S_u(z,y;A). \tag{13}$$

The kernel $\vec{\gamma}\cdot\vec{D}$ is responsible for hopping in the spatial direction. The full solution can be obtained by substituting S_u^0 for S_u iteratively, leading to a hopping expansion series

$$\begin{aligned}S_u(x,y;A)=&S_u^0(x,y;A_4)\\&+\int_{y_4}^{x_4}dz_4\int d^3z S_u^0(x,z;A_4)\vec{\gamma}\cdot\vec{D}S_u^0(z,y;A_4)\\&+\int_{y_4}^{x_4}dz_4'\int_{y_4}^{z_4'}dz_4\int d^3z'd^3z S_u^0(x,z';A_4)\\&\times\vec{\gamma}\cdot\vec{D}S_u^0(z',z;A_4)\vec{\gamma}\cdot\vec{D}S_u^0(z,y;A_4)+\cdots.\end{aligned} \tag{14}$$

It is clear from this expansion that the time integration variables $z_4',z_4,\ldots$ are sequenced between x_4 and y_4 due to θ and δ functions in Eq. (12). A typical term in the series is shown graphically in Fig. 6.

From this we see that there is no time-backward propagation in $S_u(x,y;A)$. Therefore, there is no pair creation or annihilation in the particle propagator, although it still propagates forward and backward in the spatial direction. Similarly, one can show that the antiparticle propagator $S_v(x,y;A)$ contains only time-backward propagation.

Although there is no pair creation or annihilation in VQCD, there are still quark loops in the spatial direction which could lead to nontrivial dynamical effects via the fermion determinant. Since we want to emulate the valence quark model, the sea degree of freedom needs to be removed also. By the same token, we will not include the fermion determinant in the calculation. In other words, both quark loops associated with the external currents and the internal quark loops associated with the determinant are dropped in the present study.

A. Pauli spinor representation

In the process of replacing the fermion field Ψ in QCD by two Dirac spinors u and v in VQCD, we seem to have doubled the degrees of freedom. It turns out that half of the degrees of freedom in u and v are not dynamical and thus can be integrated out. As a result, VQCD can be represented by Pauli spinor fields. To prove this, we first look at the particle part of the fermion action from the VQCD Lagrangian in Eq. (9) and write it in terms of the upper and lower components:

$$\begin{aligned}S_u=&\int d^4x(\overline{u_1}\,\overline{u_2})\begin{pmatrix}D_4+m & i\vec{\sigma}\cdot\vec{D}\\ -i\vec{\sigma}\cdot\vec{D} & m\end{pmatrix}\begin{pmatrix}u_1\\u_2\end{pmatrix}\\=&\int d^4x\left[\overline{u_1}\left(D_4+m-\frac{(\vec{\sigma}\cdot\vec{D})^2}{m}\right)u_1\right.\\&\left.+\left(\overline{u_2}+\overline{u_1}\frac{i(\vec{\sigma}\cdot\vec{D})}{m}\right)m\left(u_2+\frac{-i(\vec{\sigma}\cdot\vec{D})}{m}u_1\right)\right].\end{aligned} \tag{15}$$

After changing the field variables $u_1\to\chi_1$, and $u_2+[-i(\vec{\sigma}\cdot\vec{D})/m]u_1\to\xi_1$, the action becomes

$$S_u=\int d^4x\left[\overline{\chi_1}\left(D_4+m-\frac{(\vec{\sigma}\cdot\vec{D})^2}{m}\right)\chi_1+\overline{\xi_1}m\xi_1\right]. \tag{16}$$

Since the $\overline{\xi_1}m\xi_1$ part has no dynamics and is quadratic, it can be integrated out, leaving the particle action represented by the Pauli spinor χ_1:

$$S_u=\int d^4x\overline{\chi_1}\left(D_4+m-\frac{\vec{D}^2+\vec{\sigma}\cdot\vec{B}}{m}\right)\chi_1. \tag{17}$$

Similarly, the antiparticle action S_v can also be written in terms of the Pauli spinor:

$$S_v=\int d^4x\overline{\chi_2}\left(-D_4+m-\frac{\vec{D}^2+\vec{\sigma}\cdot\vec{B}}{m}\right)\chi_2. \tag{18}$$

We can redefine the Dirac spinor as

$$\chi=\begin{pmatrix}\chi_1\\\chi_2\end{pmatrix}$$

and rewrite the VQCD Lagrangian as

$$\mathcal{L}_{VQCD}=-\frac{1}{4}F_{\mu\nu}F_{\mu\nu}-\chi\left(\gamma_4 D_4+m-\frac{\vec{D}^2+\vec{\sigma}\cdot\vec{B}}{m}\right)\chi$$

$$=-\frac{1}{4}F_{\mu\nu}F_{\mu\nu}-(\chi_1\chi_2)\begin{pmatrix} D_4+m-\dfrac{\vec{D}^2+\vec{\sigma}\cdot\vec{B}}{m} & 0 \\ 0 & -D_4+m-\dfrac{\vec{D}^2+\vec{\sigma}\cdot\vec{B}}{m}\end{pmatrix}\begin{pmatrix}\chi_1\\ \chi_2\end{pmatrix}. \tag{19}$$

It is clear from Eq. (19) that particle field χ_1 and antiparticle field χ_2 decouple. This also proves that $\mathcal{L}_{VQCD}$ in Eq. (9) does not double the fermion degrees of freedom (DOF). After integrating out the nondynamical DOF it has exactly four propagating spinors as shown in Eq. (19). It is worthwhile remarking that the Pauli form of $\mathcal{L}_{VQCD}$ in Eq. (19) resembles that of the nonrelativistic QCD Lagrangian after Foldy-Wouthuysen transformation. It has a single time derivative like in the Schrödinger action and it contains the $(\vec{D}^2+\vec{\sigma}\cdot\vec{B})/m$ term, much like the nonrelativistic expansion. However, we should stress that the Pauli form of VQCD is *not* a nonrelativistic or other expansion. Its form is exact. Furthermore, it does not have spin-orbit, tensor, and Darwin terms as in nonrelativistic QCD.

B. Discrete symmetry

Let us explore the symmetries of VQCD and see if there is any change from QCD. First we examine the discrete symmetries: parity, charge, and time reversal.

The gluon part of the VQCD is the same as in QCD and there is no need to modify the transformation of the gluon field. For parity and time reversal, the u and v fields transform the same way as Ψ in QCD. Thus in VQCD

$$P\begin{pmatrix}u(x)\\ v(x)\end{pmatrix}P^{-1}=\gamma_4\begin{pmatrix}u(x^P)\\ v(x^P)\end{pmatrix}, \tag{20}$$

$$T\begin{pmatrix}u(x)\\ v(x)\end{pmatrix}T^{-1}=\sigma_2\begin{pmatrix}u(x^T)\\ v(x^T)\end{pmatrix}, \tag{21}$$

where $x^P=(-\vec{x},x_4)$, $x^T=(\vec{x},-x_4)$. It is easy to show that the VQCD action $S_{VQCD}=\int d^4x\mathcal{L}_{VQCD}$ is invariant under the above parity and time reversal transformations.

As for the charge transformation, we need to take into account the fact that u and v are particle and antiparticle fields which should be transformed into each other under charge transformation. We find that S_{VQCD} is invariant under the following charge transformation:

$$C\begin{pmatrix}u_\alpha\\ v_\alpha\end{pmatrix}C^{-1}=\begin{pmatrix}(\gamma_2)_{\alpha\beta}v^\dagger_\beta\\ (\gamma_2)_{\alpha\beta}u^\dagger_\beta\end{pmatrix}. \tag{22}$$

Thus, with the appropriate definition, VQCD satisfies the C, P, and T invariance.

C. Continuous symmetry: U($2N_F$)

Next, we shall address the continuous symmetries. Since the Dirac structure of the time derivative is modified in VQCD, it is no longer Lorentz invariant, although it is still translational invariant. This should be acceptable for the purpose of our study, i.e., hadron physics at low energy and small momentum transfer. After all, the quark model is supposed to be an effective theory of low energy and small momentum transfer, unlike the parton model which addresses different kinetic regimes.

As in QCD, VQCD has global vector and axial symmetries. It is invariant under the U(1) transformation

$$u\to e^{i\alpha}u,\quad v\to e^{i\alpha'}v. \tag{23}$$

This leads to the conserved vector currents

$$\partial_\mu J^u_\mu=0,\quad \partial_\mu J^v_\mu=0, \tag{24}$$

where the Noether currents associated with these gauge transformations are

$$J^u_\mu=\bar{u}\begin{pmatrix} i\gamma_i \\ i\dfrac{\gamma_4+1}{2}\end{pmatrix}u,\quad J^v_\mu=\bar{v}\begin{pmatrix} i\gamma_i \\ i\dfrac{\gamma_4-1}{2}\end{pmatrix}v. \tag{25}$$

Therefore, the particle and antiparticle are separately conserved. This is in contrast to the conserved current $J_\mu=\bar{\Psi}i\gamma_\mu\Psi$ in QCD where only the difference of the particle and the antiparticle numbers or the valence number is conserved, i.e.,

$$N_V=\int d^3x\bar{\Psi}\gamma_4\Psi$$

$$=\int\frac{d^3p}{(2\pi)^3}\sum_s\left[b^\dagger_s(\vec{p})b_s(\vec{p})-d^\dagger_s(\vec{p})d_s(\vec{p})\right], \tag{26}$$

where $b^\dagger/d^\dagger$ and b/d are the creation and annihilation operators of particles and antiparticles in QCD.

The axial symmetry of VQCD is realized in the γ_5 transformation

$$u\to e^{i\theta\gamma_5}v,\quad v\to e^{i\theta'\gamma_5}u. \tag{27}$$

The Lagrangian $\mathcal{L}_{VQCD}$ with $m=0$ is invariant under this transformation which transposes the u and v terms in the Lagrangian. As a result, one has the conserved axial currents

$$A_\mu = i\bar{u}\begin{pmatrix} \gamma_i \\ \dfrac{\gamma_4+1}{2} \end{pmatrix}\gamma_5 v, \tag{28}$$

$$A_\mu^\dagger = i\bar{v}\begin{pmatrix} \gamma_i \\ \dfrac{\gamma_4-1}{2} \end{pmatrix}\gamma_5 u. \tag{29}$$

We should point out that there is no Adler-Bell-Jackiw anomaly [39] in VQCD. This is so because in VQCD there is no quark loop involving the time direction; hence there is no triangle diagram to generate the axial anomaly. With $m\neq 0$, the axial Ward identities are

$$\partial_\mu A_\mu = 2m\bar{u}i\gamma_5 v, \tag{30}$$

$$\partial_\mu A_\mu^\dagger = 2m\bar{v}i\gamma_5 u. \tag{31}$$

It is useful to consider the particle field u and antiparticle field v as two flavors and define

$$\zeta = \begin{pmatrix} u \\ v \end{pmatrix};$$

then the VQCD Lagrangian in Eq. (9) can be written as

$$\mathcal{L}_{VQCD} = -\frac{1}{4}F_{\mu\nu}F_{\mu\nu} - \bar{\zeta}\left[\frac{\gamma_4+\tau_3}{2}D_4 + \vec{\gamma}\cdot\vec{D} + m\right]\zeta. \tag{32}$$

At the massless limit, VQCD is invariant under the transformation

$$\zeta \to e^{i\alpha I}\zeta, \quad \zeta \to e^{i\alpha'\tau_3}\zeta, \quad \zeta \to e^{i\theta\gamma_5\tau_1}\zeta, \quad \zeta \to e^{i\theta\gamma_5\tau_2}\zeta, \tag{33}$$

where τ's are the Pauli spinor in the two-component u,v space. The four operators I, τ_3, $\gamma_5\tau_1$, and $\gamma_5\tau_2$ are the generators of the U(2) algebra. So massless VQCD has U(2) vector and axial symmetries in the particle-antiparticle space. For degenerate massless N_F flavors, it has U($2N_F$) symmetry. This is in contrast to the SU(N_F)$_L\times$SU(N_F)$_R\times$U$_V$(1) chiral and U$_V$(1) symmetry of QCD. In VQCD with N_F flavors, the charges $Q_\pm^a = \int d^3x[\bar{u}\gamma_4(t^a/2)u \pm \bar{u}\gamma_4\gamma_5(t^a/2)v]$ do not form a complete SU(N_F)$\times$SU(N_F) algebra because the vector and axial currents contain different fields. This can also be seen from the states. For massless particle, u satisfies the Dirac equation

$$\left[\frac{\gamma_4+1}{2}D_4 + \vec{\gamma}\cdot\vec{D}\right]u = 0, \tag{34}$$

and $\gamma_5 v$ satisfies the same equation:

$$\left[\frac{\gamma_4+1}{2}D_4 + \vec{\gamma}\cdot\vec{D}\right](\gamma_5 v) = 0. \tag{35}$$

Therefore, $\chi_\pm = \frac{1}{2}(u\pm\gamma_5 v)$ is a solution of the Dirac equation in Eq. (34), but it has different particle content; i.e., it is a mixture of particles and antiparticles. As a result, $\chi_\pm$ does not have a definite handedness, it contains both helicity states. From this we conclude that massless VQCD does not have SU(N_F)$_L\times$SU(N_F)$_R$ chiral symmetry as in QCD. Instead, it has the vector-axial U($2N_F$) in the flavor and particle-antiparticle space.

D. Zero-quark-mass limit

Even though we have explored the axial symmetry of VQCD in Sec. III C in the massless limit, there is a concern that the the zero-quark-mass limit may be singular. This can be seen from the Dirac equation for a free quark. From Eq. (34),

$$\begin{pmatrix} \partial_4 & \vec{\sigma}\cdot\vec{\partial} \\ \vec{\sigma}\cdot\vec{\partial} & 0 \end{pmatrix}\begin{pmatrix} u_1 \\ u_2 \end{pmatrix} = 0. \tag{36}$$

This leads to two Laplace equations for the upper and lower components of the particle field u:

$$\nabla^2 u_1 = 0, \quad \nabla^2 u_2 = 0. \tag{37}$$

There are no time derivatives in these constraint equations and thus no dynamics [40]. Similarly, ones sees that the ξ field in Eq. (16) is ill defined for the $m=0$ case.

To address this problem, we consider the following approach. Let us consider the fermion part of the VQCD Lagrangian with a small admixture of antiparticle part in the particle action and vice versa,

$$\mathcal{L}_F = -\bar{u}\left[\frac{\gamma_4+1}{2}D_4 + \epsilon\frac{\gamma_4-1}{2}D_4 + m + \vec{\gamma}\cdot\vec{D}\right]u - \bar{v}\left[\frac{\gamma_4-1}{2}D_4 + \epsilon\frac{\gamma_4+1}{2}D_4 + m + \vec{\gamma}\cdot\vec{D}\right]v, \tag{38}$$

and then let both m and ϵ go to zero.

Let us first consider the free quark case. In this case, the fermion Lagrangian is

$$\mathcal{L}'_F = -\bar{u}\begin{pmatrix} \partial_4+m & \vec{\sigma}\cdot\vec{\partial} \\ \vec{\sigma}\cdot\vec{\partial} & -\epsilon\partial_4+m \end{pmatrix}u - \bar{v}\begin{pmatrix} \epsilon\partial_4+m & \vec{\sigma}\cdot\vec{\partial} \\ \vec{\sigma}\cdot\vec{\partial} & -\partial_4+m \end{pmatrix}v. \tag{39}$$

This involves two time derivatives. The eigenvalues for u are determined from

$$det\begin{pmatrix} -E+m & i\vec{\sigma}\cdot\vec{p} \\ i\vec{\sigma}\cdot\vec{p} & \epsilon E+m \end{pmatrix} = 0, \tag{40}$$

which are, for small ϵ,

$$E = m + \frac{\vec{p}^2}{m}, \tag{41}$$

$$E = -\frac{m(1-\epsilon)}{\epsilon} - \left(m + \frac{\vec{p}^2}{m} \right). \tag{42}$$

Note that in Eq. (41) the kinetic energy term $\vec{p}^2/m$ is different from $\vec{p}^2/2m$ in the nonrelativistic case. Now if we let ϵ approach zero faster than m, the second branch in Eq. (42) will be decoupled from the physical spectrum. However, at the massless limit, a gap between $E=p=0$ and $E=\infty$ is generated from Eq. (41). This could pose a problem for perturbation treatment around this axially symmetric point.

However, the situation is modified when the quarks are interacting. In this case, the Dirac equation for u is

$$\begin{pmatrix} D_4 + m & i\vec{\sigma}\cdot\vec{D} \\ i\vec{\sigma}\cdot\vec{D} & -\epsilon D_4 + m \end{pmatrix} \begin{pmatrix} u_1 \\ u_2 \end{pmatrix} = 0. \tag{43}$$

One of the coupled equation from Eq. (43) is

$$\left(D_4^2 - \frac{m}{\epsilon}(1-\epsilon)D_4 - \frac{m^2}{\epsilon} \right) u_2 = \frac{(\vec{D}^2 + \vec{\sigma}\cdot\vec{B})u_2 + ig\vec{\sigma}\cdot\vec{E}u_1}{\epsilon}. \tag{44}$$

If we let m and ϵ approach zero at the same rate such that $m/\epsilon = \lambda \gg \lambda_{QCD}$, the right-hand side of Eq. (44) leads to a constraint equation

$$(\vec{D}^2 + \vec{\sigma}\cdot\vec{B})u_2 + ig\vec{\sigma}\cdot\vec{E}u_1 = 0, \tag{45}$$

and the left-hand side leads to two equations, both with linear time dependence:

$$D_4 u_2 = 0, \tag{46}$$

$$(D_4 - \lambda)u_2 = 0. \tag{47}$$

Since $\lambda \gg \lambda_{QCD}$, the solution from Eq. (47) is decoupled from the physical system of the hadrons.

Therefore, the Dirac equation for the massless interacting quark with the ϵ regulator leads to the following coupled equations:

$$D_4 u_1 + i\vec{\sigma}\cdot\vec{D}u_2 = 0, \tag{48}$$

$$D_4 u_2 = 0, \tag{49}$$

with Eq. (45) as a constraint. This should admit propagating solutions. A similar situation exists for v. Thus, we can approach the interacting massless quark case with the help of the infrared ϵ regulator.

IV. LATTICE VQCD

In order to solve VQCD, we devise a lattice version of the theory. The lattice VQCD action is based on Wilson's action in QCD and takes the form

$$S^L_{VQCD} = S_G + S^u_F + S^v_F, \tag{50}$$

where S_G is Wilson's gauge action and the quark action S^u_F and the antiquark action S^v_F are

$$S^u_F = \sum_x \Big\{ \overline{u}(x)u(x) - \kappa[\overline{u}(x+a_4)(1+\gamma_4)U^\dagger_4(x)u(x) + u_0\overline{u}(x)(1-\gamma_4)u(x)] - \kappa\sum_i [\overline{u}(x+a_i)(1+\gamma_i)U^\dagger_i(x)u(x) + \overline{u}(x)(1-\gamma_i)U_i(x)u(x+a_i)] \Big\}, \tag{51}$$

$$S^v_F = \sum_x \Big\{ \overline{v}(x)v(x) - \kappa[\overline{v}(x)(1-\gamma_4)U_4(x)v(x+a_4) + u_0\overline{v}(x)(1+\gamma_4)v(x)] - \kappa\sum_i [\overline{v}(x+a_i)(1+\gamma_i)U^\dagger_i(x)v(x) + \overline{v}(x)(1-\gamma_i)U_i(x)v(x+a_i)] \Big\}, \tag{52}$$

with u_0, the tadpole contribution of the gauge link U_μ, taken to be $(\mathrm{Tr}\,\Box)^{1/4}$ [41]. This has VQCD in Eq. (9) as the classical continuum limit.

A. Reflection positivity and Hermiticity

Similar to the continuum case in Sec. III B, the lattice VQCD action in Eq. (50) is invariant under the corresponding lattice C, P, and T transformations.

For Euclidean action, it is imperative that it satisfy Osterwalder-Schrader reflection positivity [42] in order to allow the Euclidean correlations to be continued back to the Minkowski space. We shall follow the derivation for the Wilson action [43]. To prove reflection positivity, one needs to show

$$\langle (\Theta F)F \rangle \geqslant 0, \tag{53}$$

where F is a function of the fields $\overline{u}$, u, $\overline{v}$, v, and U on the positive time part of the lattice and Θ is the time reflection operator. We shall consider the ''link-reflection'' case where the time reflection is with respect to the $t=(0\rightarrow 1)$ link. In this case, Θ is defined by the transformation

$$\Theta u_{x,t} = \overline{u}_{x,1-t}\gamma_4, \quad \Theta\overline{u}_{x,t} = \gamma_4 u_{x,1-t}, \tag{54}$$

$$\Theta v_{x,t} = \overline{v}_{x,1-t}\gamma_4, \quad \Theta\overline{v}_{x,t} = \gamma_4 v_{x,1-t}, \tag{55}$$

$$\Theta U(x,t_x;y,t_y)=U^{\dagger}(x,1-t_x;y,1-t_y). \tag{56}$$

We shall prove the reflection positivity for the u part of the action. The proof can be extended similarly to include the v field. Denoting the field variables in the half-space with positive time $t\geqslant 1$ by $u^{+},\overline{u}^{+},U^{+}$, and in the other half-space with $t\leqslant 0$ by $u^{-},\overline{u}^{-},U^{-}$, the u part of the VQCD action can be separated into three parts:

$$S_{VQCD}=S_{+}[\overline{u}^{+},u^{+},U^{+}]+S_{-}[\overline{u}^{-},u^{-},U^{-}]+S_{c}[\overline{u}^{+},u^{-}], \tag{57}$$

where

$$S_{c}[\overline{u}^{+},u^{-}]=-\kappa\sum_{\vec{x}}\ [\overline{u}^{+}_{\vec{x},1}(1+\gamma_4)u^{-}_{\vec{x},0}] \tag{58}$$

is the action which connects S_{+} and S_{-} and involves links between $t=0$ and $t=1$. Here we have used the temporal gauge. Because of the fact that

$$\begin{aligned}\Theta S_{+}[\overline{u}^{+},u^{+},U^{+}]&=S_{+}^{\dagger}[\Theta\overline{u}^{+},\Theta u^{+},\Theta U^{+}]\\&=S_{-}[\overline{u}^{-},u^{-},U^{-}],\end{aligned} \tag{59}$$

the integral in Eq. (53) is then

$$\begin{aligned}\langle(\Theta F)F\rangle=Z^{-1}\int dU d\overline{u}^{+}du^{+}&\\ \times e^{-S_{+}[\overline{u}^{+},u^{+},U^{+}]}F[\overline{u}^{+},u^{+},U^{+}]&\\ \times\int d(\Theta\overline{u}^{+})d(\Theta u^{+})&\\ \times e^{-S_{+}^{\dagger}[\Theta\overline{u}^{+},\Theta u^{+},\Theta U^{+}]}F^{\dagger}[\Theta\overline{u}^{+},\Theta u^{+},\Theta U^{+}]&\\ \times\exp\left(-\kappa\sum_{\vec{x}}\ \overline{u}^{+}_{\vec{x},1}(\gamma_4+1)(\Theta\overline{u}^{+}_{\vec{x},1})\right).&\end{aligned} \tag{60}$$

Consider the Taylor expansion of the last exponential in Eq. (60):

$$1-\kappa\sum_{\vec{x}}\ \overline{u}^{+}_{\vec{x},1}(\gamma_4+1)(\Theta\overline{u}^{+}_{\vec{x},1})+\cdots. \tag{61}$$

The only terms that survive the Grassmann integration are the first two terms and, with a diagonal representation of γ_4, they give semipositive definite contributions to $\langle(\Theta F)F\rangle$. Extension to include the v field is straightforward and thus the reflection positivity for the VQCD action is proved.

In constructing meson propagators, the usual practice is to first invert the quark matrix to obtain the quark propagator from the source to all lattice points, i.e., $M^{-1}(x,0)$. Then the antiquark propagator which goes backward in time is obtained through the Hermiticity relation

$$M^{-1\dagger}(0,x)=\gamma_5 M^{-1}(x,0)\gamma_5, \tag{62}$$

where $\dagger$ indicates the Hermitian conjugation in the color and Dirac indices. In VQCD, a similar situation exists. In constructing a $q\overline{q}$ meson, one needs the quark propagator $M_u^{-1}(x,0)$ and the antiquark propagator $M_v^{-1}(0,x)$. It turns out that the Hermiticity relation

$$M_v^{-1\dagger}(0,x)=\gamma_5 M_u^{-1}(x,0)\gamma_5 \tag{63}$$

still exists, so that one can obtain the antiquark propagator from the quark to construct a meson propagator as before.

B. Free quark propagator

It is useful to understand the free quark spectrum and its residue at the pole for the lattice VQCD and see how different they are from the Wilson and the continuum ones. The inverse of the free quark propagator of VQCD in momentum space is

$$\begin{aligned}S_F^{u\,-1}(p)=1-\kappa(1-\gamma_4)-\kappa(1+\gamma_4)e^{-ip_4a}&\\ -\kappa\sum_i\ [(1+\gamma_i)e^{-ip_ia}+(1-\gamma_i)e^{ip_ia}],&\end{aligned} \tag{64}$$

where a is the lattice spacing. We can compute the propagator in discrete time $t=n_ta$:

$$S_F^u(t,\vec{p})=\int_{-\pi}^{\pi}\frac{dp_4}{2\pi}S_F^u(p)e^{ip_4t}. \tag{65}$$

For $n_t>0$ and $\vec{p}$ in the three-direction,

$$\begin{aligned}S_F^u(t,p_3)=\frac{e^{-Et}}{B}[A-\kappa e^{Ea}+\kappa(e^{Ea}-1)\gamma_4&\\ -2i\kappa\gamma_3\sin(p_3a)],&\end{aligned} \tag{66}$$

where

$$\begin{aligned}A&=1-5\kappa-2\kappa\cos(p_3a),\\ B&=A^2-\kappa^2+4\kappa^2\sin^2(p_3a),\\ Ea&=\ln\left(\frac{B}{2A\kappa-2\kappa^2}\right),\end{aligned} \tag{67}$$

and E is the energy. For small p_3a, i.e., $p_3a\ll 1$,

$$Ea=\overline{m}a+\frac{ma+2}{2ma(ma+1)}(p_3a)^2, \tag{68}$$

where

$$\overline{m}a=\ln\left(\frac{1-6\kappa}{2\kappa}\right) \tag{69}$$

is the free quark mass which is the same as in the Wilson case and $ma=1/2\kappa-4$ is the small mass approximation for $\overline{m}a$.

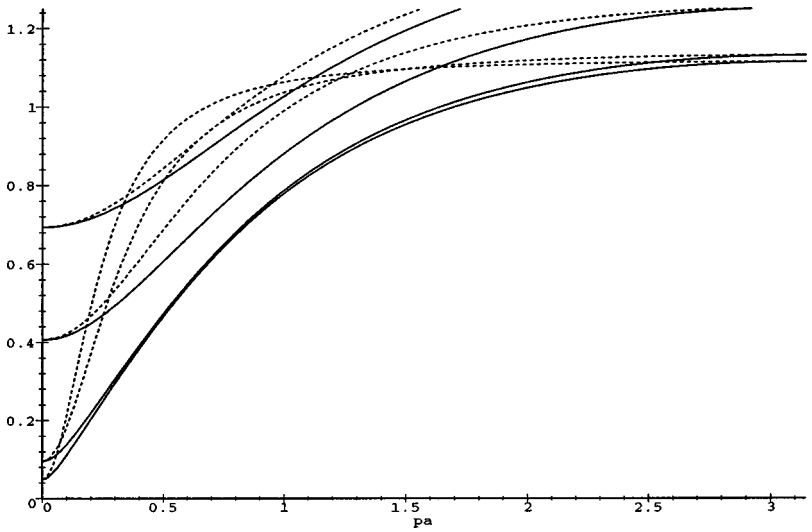

FIG. 7. The dispersion relations between Ea and $p_3 a$ for a free quark are compared between the Wilson (solid lines) and the lattice VQCD (dashed lines) version for $ma=0.05$, 0.1, 0.5, and 1.0.

We plot in Fig. 7, the dispersion relation of Ea vs $p_3 a$ for a range of ma ($ma=0.05$, 0.1, 0.5, and 1.0) for both the valence (dashed lines) and the Wilson case (solid lines). We see that for heavy quarks, i.e., $ma=0.5$ and 1, the two curves at the top are close to each other. But they differ at small mass and low momentum. At small $p_3 a$, the behavior of Eq. (68) holds for the valence case. At $ma=\bar{m}a=0$, there is a singularity at $Ea=p_3 a=0$. For any finite $p_3 a$, $Ea=\ln 3$ which resembles the infinite gap in the free massless quark situation in the continuum [see Eq. (41)].

Finally, we see that at zero momentum the static propagator is

$$S(t>0,\vec{p}=0)=\frac{1}{1-6\kappa}e^{-\bar{m}t}\frac{1+\gamma_4}{2}. \tag{70}$$

This is the same as in the Wilson case and the wave function normalization factor $1/(1-6\kappa)$ is also the same. To convert lattice matrix elements of local currents with bilinear quark fields, e.g., $\bar{\Psi}(x)\Gamma\Psi(x)$, to the continuum ones, besides the finite lattice renormalization one needs to multiply the factor $(1-6\kappa u_0)/2\kappa=u_0 e^{m_q a}$ to take into account the finite mass normalization due to the Wilson quark action with tadpole improvement [41,45]. Here $u_0=1/8\kappa_c$ where κ_c is the critical κ at which point the pion mass is zero and $m_q a=\ln(1/2\kappa u_0-3)$ is the tadpole-improved definition of the bare quark mass in Eq. (69).

C. Lattice details

We use the same gauge configurations which have been used for the study of hadron masses, matrix elements, and form factors [45,46,20,21,47] in the quenched approximation. This way we keep the scale of the lattice spacing unchanged. These quenched gauge configurations were generated on a $16^3\times 24$ lattice at $\beta=6.0$. The gauge field was thermalized for 5000 pseudo-heat-bath sweeps from a cold start and 100 configurations separated by at least 1000 sweeps were used. Periodic boundary conditions were imposed on the quark fields in the spatial directions. In the time direction, fixed boundary conditions were imposed on the quarks to provide larger time separations than available with periodic boundary conditions. All quark propagators in the quenched approximation were chosen to originate from lattice time slice 5; the secondary nucleon source was fixed at time slice 20 (except for $\kappa=0.154$ where the quark propagators from time slice 3 to 22 were used). In the case of VQCD, all quark propagators originate from time slice 2 and terminate at time slice 22 for the three-point function calculation. We also averaged over the directions of equivalent lattice momenta in each configuration; this reduces error bars.

We have verified that the time separation is sufficient so that there is a plateau for the quark bilinear current insertion at time slices t_1 after the nucleon ground state is achieved. The quenched approximation part is done for the lightest quarks with $\kappa=0.154$, 0.152, 0.148, and 0.140, and $\vec{q}^{\,2}a^2$ up to $4(2\pi/L)^2$. The nucleon masses $M_N a$ for $\kappa=0.154$, 0.152, and 0.148 are 0.731(11), 0.883(9), and 1.153(7), respectively. The corresponding pion masses $m_\pi a$ are 0.375(4), 0.487(3), and 0.679(3). Extrapolating the nucleon and pion masses to the chiral limit where we determine $\kappa_c=0.15672(4)$ and the nucleon mass at the chiral limit to be 0.536(13). Using the nucleon mass to set the scale which we believe to be appropriate for studying nucleon properties [45,46,20], the lattice spacing $a^{-1}=1.75(2)$ GeV is determined. The three κ's then correspond to quark masses of about 120, 205, and 370 MeV, respectively.

Since we use the same gauge configurations for VQCD, the lattice spacing is the same as that in the quenched approximation. This is certainly obvious if we choose the string tension or the glueball mass to set the scale. Using the physical nucleon mass to set the scale in the quenched approximation opens up the question as to what extent the fermion determinant effects are implicitly included. It is shown [48] that the quenched approximation can be viewed as including

leading terms in the loop expansion of the fermion determinant which are commensurate with the size of loops in the gauge action. This leads to a shift in β or the coupling constant. However, when the infinite volume and continuum limits are taken [49], the scales set by hadron masses and by the string tension are consistent. Since we are not at the infinite volume and continuum limits, the scales differ by $\sim 20\%$. Nevertheless, whatever scale we decide to choose, the lattice spacing is the same in the following VQCD calculations as in our quenched QCD results.

The determination of κ_c which corresponds to the zero quark mass will be discussed in the next section. To determine the finite quark mass, we shall use the tadpole-improved form of the lattice free quark mass in Eq. (69), i.e.,

$$m_q a = \ln\left(\frac{1}{2\kappa u_0} - 3\right) = \ln\left(\frac{4\kappa_c}{\kappa} - 3\right), \tag{71}$$

where we have used $u_0 = 1/8\kappa_c$.

D. Pion decay constant, pion mass, and κ_c

The pion decay constant f_π plays an essential role in low-energy chiral dynamics. It sets the scale for chiral perturbation theory and relates the Goldstone boson mass to the quark mass through the Gell-Mann–Oakes-Renner relation [44]

$$f_\pi^2 m_\pi^2 = -(m_u + m_d)\langle \bar{q}q \rangle, \tag{72}$$

where $\langle \bar{q}q \rangle$ is the quark condensate, which is the order parameter for chiral symmetry breaking. In VQCD, it is not clear if there is a corresponding relation or, more importantly, if the U($2N_f$) symmetry is broken to generate Goldstone bosons. We can, however, look for clues from the pion decay matrix element with the axial current. In QCD, the pion decay constant is defined by

$$\langle 0|A_\mu(x)|\pi(p)\rangle = i f_\pi p_\mu e^{ip\cdot x}. \tag{73}$$

Applying the axial identity from Eq. (31) to the zero-momentum pion state, we obtain, in VQCD,

$$\begin{aligned}\langle 0|\partial_4 A_4^\dagger(x)|\pi(0)\rangle &= m_\pi^2 f_\pi(m_\pi) e^{-m_\pi t} \\ &= 2m\langle 0|\bar{v} i\gamma_5 u|\pi(0)\rangle e^{-m_\pi t},\end{aligned} \tag{74}$$

where m is the quark mass. From this, we find

$$m_\pi^2 \frac{f_\pi(m_\pi)}{\langle 0|\bar{v} i\gamma_5 u|\pi(0)\rangle} = 2m. \tag{75}$$

It is clear from Eq. (75) that as long as the ratio $f_\pi(m_\pi)/\langle 0|\bar{v} i\gamma_5 u|\pi(0)\rangle$ does not diverge as fast as $1/m_\pi^2$ when the quark mass approaches zero, the pion mass will go to zero in the massless quark limit. Furthermore, if the pion decay constant f_π is not zero in the massless limit, it would signal spontaneous axial symmetry breaking with the pion as the Goldstone boson. The quantities f_π, m_π and the current quark mass m are calculated by fitting the following two-point functions to

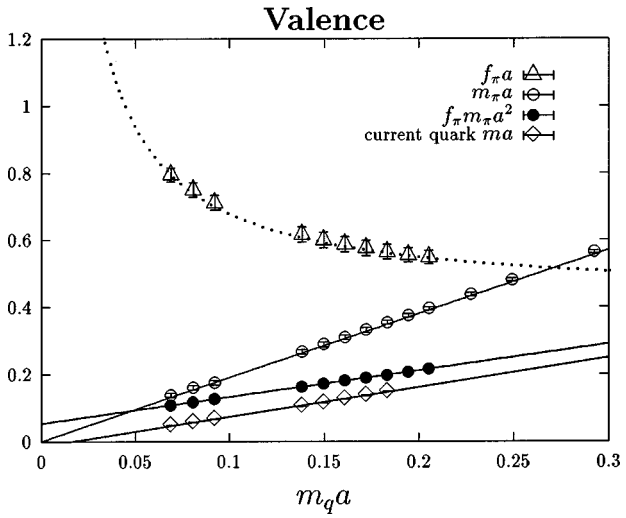

FIG. 8. The dimensionless pion mass $m_\pi a$, the current quark mass ma, and the pion decay constant $f_\pi a$ are shown as a function of $m_q a = \ln(4\kappa_c/\kappa - 3)$. The solid lines represent the linear extrapolation with respect to $m_q a$.

$$\left\langle \sum_{\vec{x}} \left[i\bar{v}\frac{\gamma_4 - 1}{2}\gamma_5 u(\vec{x},t)\right] P(0,0)\right\rangle \xrightarrow[t \gg a]{} \frac{f_\pi m_\pi Z_\pi}{2m_\pi} e^{-m_\pi t}, \tag{76}$$

$$\left\langle \sum_{\vec{x}} \left[i\partial_t \bar{v}\frac{\gamma_4 - 1}{2}\gamma_5 u(\vec{x},t)\right] P(0,0)\right\rangle \xrightarrow[t \gg a]{} \frac{2mZ_\pi^2}{2m_\pi} e^{-m_\pi t}, \tag{77}$$

$$\left\langle \sum_{\vec{x}} P(\vec{x},t)P(0,0)\right\rangle \xrightarrow[t \gg a]{} \frac{Z_\pi^2}{2m_\pi} e^{-m_\pi t}. \tag{78}$$

Here P is the pseudoscalar interpolation field $\bar{u} i\gamma_5 v$ and $Z_\pi = \langle \pi|P|0\rangle$ is the wave function overlap. We use the local current for the axial current in Eq. (76) for the lattice calculation. There are finite lattice renormalizations associated with the operators in these matrix elements. We have not calculated them, but we expect the multiplicative renormalization constants Z_A and Z_P for the axial and pseudoscalar operators to be of order 1, as in the quenched approximation. Our results presented below are subject to this caveat.

With Wilson-type fermions, one needs to find out κ_c corresponding to zero quark mass. To determine κ_c, we plot the dimensionless pion mass, the current quark mass, and the pion decay constant in Fig. 8 as a function of $m_q a = \ln(4\kappa_c/\kappa - 3)$ where κ_c is to be determined from the extrapolation. The pion mass is very linear in the range of the quark mass considered. At the same time, the pion decay constant f_π behaves like $1/m_\pi$ in this range. Since from Eq. (76) and Eq. (77)

$$f_\pi(m_\pi) m_\pi^2 = 2mZ_\pi, \tag{79}$$

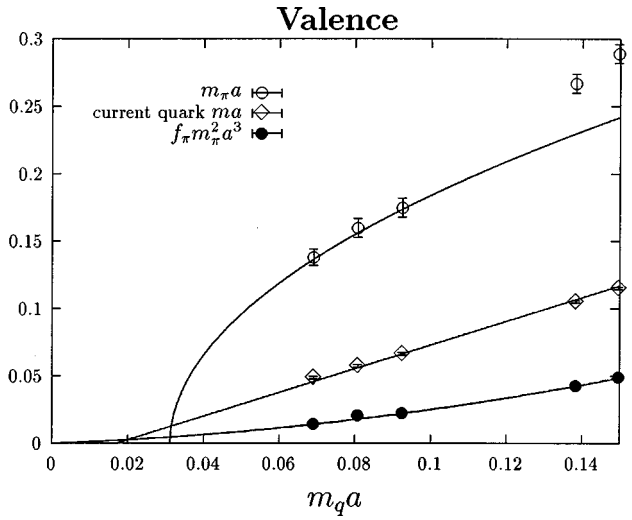

FIG. 9. The dimensionless pion mass $m_\pi a$, $f_\pi m_\pi^2 a^3$, and current quark mass ma are shown as a function of $m_q a = \ln(4\kappa_c/\kappa - 3)$ with κ_c determined from the linearly fit of m_π with respect to $m_q a$.

if the linear behavior between m_π and m persists all the way down to zero quark mass and Z_π remains constant, then f_π will diverge like $1/m_\pi$ or $1/m$. Alternatively, at smaller quark mass than we calculated here, f_π could conceivably become constant and in this case m_π would fall off like $\sqrt{m}$ as in QCD with a constant Z_π. Unfortunately, using conjugate gradient to invert the quark matrix, we have encountered critical slowing down. The smallest quark mass we run at $\kappa = 0.162$ already takes 5000 iterations to converge. It is impractical for us to go down any further. Short of theoretical guidance and numerical evidence, we extrapolate the pion mass to zero both linearly and quadratically with respect to $m_q a = \ln(4\kappa_c/\kappa - 3)$ with $\kappa = 0.162$, 0.1615, 0.1610, 0.1590, 0.1585, 0.1580, 0.1575, 0.1570, 0.1565, 0.1560, 0.155, 0.154, 0.152, and 0.148. We found that $\kappa_c = 0.1649(10)$ ($\chi^2 = 0.002$ with 14 data points) for the linear dependence and $\kappa_c = 0.1636(19)$ ($\chi^2 = 0.04$ from the three largest κ's) for the quadratic dependence. We plot in Fig. 9 the quadratic fit of m_π as a function of $m_q a$ with κ_c determined from the linear m_π fit. We see that the κ_c point from the quadratic fit crosses the abscissa at $m_q a = 0.031$; however, its error bar overlaps with that from the linear m_π fit. Also plotted in Figs. 8 and 9 is the current quark mass ma from Eq. (77) as a function of $m_q a$. Extrapolating the quark mass linearly with respect to $m_q a$, we obtain $\kappa_c = 0.1642(9)$ ($\chi^2 = 3.5$ from the first eight κ's). The covariance matrix has not been used in these extrapolations. We see that the current quark mass ma from Eqs. (75) and (77) crosses the abscissa at $m_q a = 0.017$. This is consistent with that extrapolated from the pion mass, either linearly or quadratically. The κ_c so obtained overlaps with both of the above two κ_c's within errors. It is gratifying to know that different definitions of κ_c agree. On the other hand, it does not differentiate the two scenarios of the pion mass dependence on the quark mass. We shall use the linear extrapolation with $\kappa_c = 0.1649(10)$ to define zero quark mass in this study. Also plotted in Fig. 9 is $f_\pi m_\pi^2 a^3$. We see that it is quite linear in the range of quark mass that we have considered. This confirms that $f_\pi m_\pi^2 \propto m_q$ or equivalently Eq. (79), since we have just shown in Fig. 9 that $m_q a$ and ma are linearly related. We should stress that we still do not know the behavior of the pion mass and pion decay constant when the quark mass is small. But at least we can say that f_π is nonzero (divergent or not) and m_π approaches zero at the massless quark limit. This we take to be the evidence that there is a spontaneous axial symmetry breaking with the two pions $\bar{u} i\gamma_5 v$ and $\bar{v} i\gamma_5 u$ as the Goldstone bosons for each flavor.

In VQCD, there are two quark condensates $\langle \bar{u}u \rangle$ and $\langle \bar{v}v \rangle$ which are expected to be smaller than $|\langle \bar{\Psi}\Psi \rangle|$ in QCD but nonzero due to the quark loops in the spatial direction. To the extent that they serve as the order parameter of axial symmetry breaking as suggested by the existence of the Goldstone bosons and nonvanishing f_π, the symmetry breaking seems to be weaker than in QCD. It is shown in a Schwinger-Dyson equation study [50] recently that the pseudoscalar meson mass grows either linearly or as the square root of the quark mass depending on whether it is large or small compared to a scale set by the quark condensate. The linear dependence we see between the pion mass and the quark mass in Fig. 8 may mean that the quark masses we are calculating are still larger than the scale set by the quark condensate $\langle \bar{u}u \rangle$ and $\langle \bar{v}v \rangle$ and the quadratic pion mass dependence of the quark mass may yet to set in at smaller quark masses. Either way, the nonzero $\langle \bar{u}u \rangle$ and $\langle \bar{v}v \rangle$ supports the spontaneous axial symmetry breaking scenario with two Goldstone pions.

V. SU(6) RELATIONS IN HADRON STRUCTURE

We shall examine the ratios of flavor-singlet coupling constants to the isovector ones for the axial and scalar currents and the neutron to proton magnetic moment ratio μ^n/μ^p and compare them to those in QCD. In VQCD, the sea quark contributions [e.g., Fig. 3(c)] are scrapped. In addition, the cloud quarks associated with Z graphs in the connected insertions [Figs. 3(a) and 3(b)] are excluded. As a result, we shall see that approximate SU(6) relations emerge from these ratios.

A. Axial-vector couplings, R_A, and F_A/D_A

The polarized DIS experiments [51–53] found a surprisingly small flavor-singlet axial coupling constant g_A^0 [0.27(10) [52] and 0.28(16) [53]]. Being the quark spin content of the nucleon, i.e., $g_A^0 = \Delta u + \Delta d + \Delta s$, this is much smaller than the expected value of unity from the nonrelativistic quark model or 0.75 from the SU(6) relation (i.e., 3/5 of the isovector coupling $g_A^3 = 1.2574$). This has attracted a lot of theoretical attention [54] and the ensuing confusion was dubbed the ''proton spin crisis.''

Direct lattice calculations of g_A^0 from the forward matrix element of the flavor-singlet axial current have been carried out and the smallness of g_A^0 is understood [20,55]. As explained in Sec. II, g_A^0 is composed of two components, i.e.,

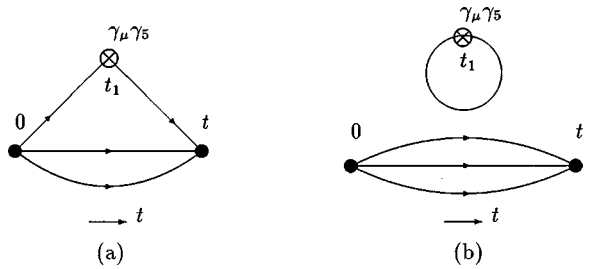

FIG. 10. Quark line diagrams of the three-point function in the Euclidean path integral formalism for evaluating g_A^0 from the flavor-singlet axial-vector current. (a) is the connected insertion which contains the valence and cloud degrees of freedom and (b) is the disconnected insertion which contains the sea quark.

$g_A^0 = g_A^0(\mathrm{CI}) + g_A^0(\mathrm{DI})$ where $g_A^0(\mathrm{CI})$ is obtained from the connected insertion in Fig. 10(a) and $g_A^0(\mathrm{DI})$ is obtained from the disconnected insertion in Fig. 10(b). Lattice calculation [20] indicates that each of the u, d, and s flavors contributes -0.12 ± 0.01 to the DI [Fig. 10(b)]. This negative vacuum polarization from the sea quarks is largely responsible for bringing the value of g_A^0 from $g_A^0(\mathrm{CI}) = 0.62(9)$ to 0.25 ± 0.12, in agreement with the experimental value (see Table I). This is an example where the sea contributes substantially and leads to a large breaking in the SU(6) relation. Thus, it is understandable that it should come as an unexpected result from the valence quark model — the latter does not have the sea degree of freedom and has simply ignored it by assuming the OZI rule.

The role of the sea is clear. How about the role of the cloud then? Since its contribution to the CI of three-point functions is entangled with the valence, we cannot separate it out as is done for the sea. To see its effect indirectly, we consider the ratio

$$R_A = \frac{g_A^0}{g_A^3} = \frac{\Delta u + \Delta d + \Delta s}{\Delta u - \Delta d} = \frac{(\Delta u + \Delta d)(\mathrm{CI}) + (\Delta u + \Delta d + \Delta s)(\mathrm{DI})}{\Delta u - \Delta d} \qquad (80)$$

as a function of the quark mass. Our results which correspond to strange and twice the charm masses are plotted in

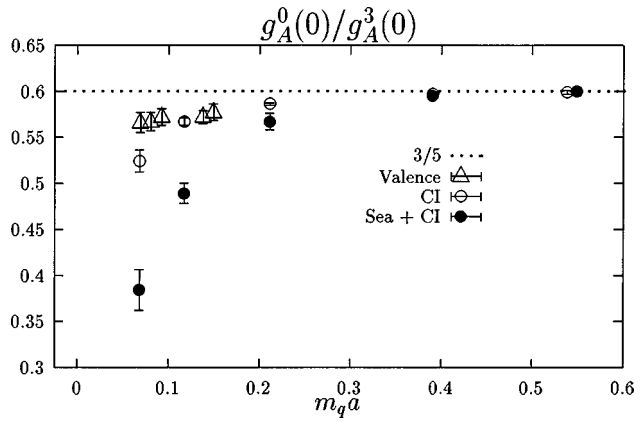

FIG. 11. The ratios R_A between flavor-singlet and isovector g_A in VQCD and QCD are plotted against the dimensionless quark mass $m_q a$ from the strange to the charm region. △ indicates the VQCD case, ○/● indicates CI/sea+CI in the QCD case. The dashed line is the SU(6) prediction of 3/5.

Fig. 11 as a function of the quark mass $m_q a = \ln(4\kappa_c/\kappa - 3)$. The dotted line is the valence quark model prediction of 3/5 for both the nonrelativistic and relativistic cases. For heavy quarks (i.e., $\kappa \geqslant 0.133$ or $ma \geqslant 0.4$ in Fig. 11), we see that the ratio R_A is 3/5 irrespective of whether the DI is included (shown as ● in Fig. 11) or not (CI alone is indicated as ○). This is to be expected because the cloud (sea) quarks which are pair produced via the Z graphs (loops) are suppressed for nonrelativistic quarks by $O(p/m_q)$ or $O(v/c)$. As for light quarks, the full result (CI+DI) is much smaller than 3/5 largely due to the negatively polarized sea contribution in the DI (Table I lists the results at the chiral limit.) Even for the CI alone, R_A still dips under 3/5. As we shall see later this is caused by the cloud quarks.

Now, we turn to the VQCD case. The same 100 gauge configurations used for quenched QCD calculation are used for the VQCD case. Since in VQCD there is only CIs [Fig. 10(a)], the R_A ratio in Eq. (80) becomes

$$R_A = \frac{g_A^0}{g_A^3}(\mathrm{CI}) = \frac{(\Delta u + \Delta d)(\mathrm{CI})}{(\Delta u - \Delta d)(\mathrm{CI})}. \qquad (81)$$

TABLE I. Axial coupling constants and quark spin contents of proton in comparison with experiments, the nonrelativistic quark model (NRQM), and the relativistic quark model (RQM).

	CI	CI + DI	Experiments	NRQM	RQM
$g_A^0 = \Delta u + \Delta d + \Delta s$	0.62(9)	0.25(12)	0.28(16) [53], 0.27(10) [52]	1	0.754
$g_A^3 = \Delta u - \Delta d$	1.20(10) [45]	1.20(10)	1.2573(28)	5/3	1.257
$g_A^8 = \Delta u + \Delta d - 2\Delta s$	0.62(9)	0.61(13)	0.579(25) [56]	1	0.754
Δu	0.91(10)	0.79(11)	0.82(5) [53], 0.82(6) [52]	4/3	1.01
Δd	−0.29(10)	−0.42(11)	−0.44(5) [53], 0.44(6) [52]	−1/3	−0.251
Δs		−0.12(1)	−0.10(5) [53], −0.10(4) [52]	0	0
$F_A = (\Delta u - \Delta s)/2$	0.45(6)	0.45(6)	0.459(8) [56]	2/3	0.503
$D_A = (\Delta u - 2\Delta d + \Delta s)/2$	0.75(11)	0.75(11)	0.798(8) [56]	1	0.754
F_A/D_A	0.60(2)	0.60(2)	0.575(16) [56]	2/3	2/3

TABLE II. Scalar contents $\sigma_{\pi N}$, F_S, and D_S in comparison with phenomenology and quark model (QM). The 17.7 MeV in the last column is determined with the quark mass from the lattice calculation.

	CI	CI + DI	Phenomenology	QM
$\langle p\|\bar{u}u+\bar{d}d\|p\rangle$	3.02(9)	8.43(24)		$\leqslant 3$
$\langle p\|\bar{u}u-\bar{d}d\|p\rangle$	0.63(9)			$\leqslant 1$
$\langle N\|\bar{s}s\|N\rangle$	1.53(7)			0
F_S	0.91(13)	1.51(12)	1.52 [61,62]—1.81 [63]	$\leqslant 1$
D_S	−0.28(10)	−0.88(28)	−0.52 [61,62]—−0.57 [63]	0
$\sigma_{\pi N}$	17.8(5) MeV	49.7(2.6) MeV	45 MeV [58]	$\leqslant$17.7 MeV

The results are plotted in Fig. 11 as a function of the dimensionless quark mass $m_q a$ (with $\kappa=0.162$, 0.1615, 0.1610, 0.1590, and 0.1585) in comparison with the QCD case. We see that, even for light quarks in the strange region ($m_q a \sim 0.07$), it is much closer to the valence prediction of 3/5, in contrast to the QCD calculation with CI alone. This shows that VQCD indeed seems to confirm our expectation of the valence quarks behavior, i.e., obeying the SU(6) relation. The deviation from the exact 3/5 prediction in Fig. 11 reflects the fact that there is still a spin-spin interaction between the valence quarks as evidenced in the $\vec{\sigma}\cdot\vec{B}$ term in the VQCD action with Pauli spinors in Eq. (17). Its effect, however, appears to be small. This also confirms our earlier assertion that the deviation of the CI of R_A in QCD (○ in Fig. 11) is largely due to the the cloud quark-antiquark pairs.

With only the CI, the F_A/D_A ratio is related to VQCD R_A in Eq. (81):

$$\frac{F_A}{D_A}(\mathrm{CI})=\frac{1+R_A}{3-R_A}. \tag{82}$$

From $R_A=0.566(11)$ for the smallest quark mass ($\kappa=0.162$), we obtain $F_A/D_A=0.643(4)$. The fact that this is only slightly larger than the QCD prediction of 0.60(2) for the CI (see Table I) has to do with the fact that the sea contribution is essentially independent of flavor in our calculation, i.e., $\Delta u_s=\Delta d_s=\Delta s$ [20]. As a result, F_A, D_A, and the F_A/D_A ratio are identical with or without the sea quarks from the DI (see Table I) and they do not reflect the large sea effect due to the individual flavor.

B. Scalar matrix elements, R_S, and D_S/F_S

A similar situation exists for the scalar current matrix elements. It has been suggested that the well-known $\pi N\sigma$ term [$\sigma_{\pi N}=\hat{m}\langle N|\bar{u}u+\bar{d}d|N\rangle$ with $\hat{m}=(m_u+m_d)/2$] puzzle [57,58] can be resolved because of the large OZI violating contribution from the sea with a large $\bar{s}s$ content in the nucleon [57,59] such that $y=2\langle N|\bar{s}s|N\rangle/\langle N|\bar{u}u+\bar{d}d|N\rangle \sim 0.2-0.3$. This has been verified in lattice calculations [60,21] which show that the DI is ~1.8 times of the CI (see Table II) [21] and the y ratio as large as 0.36 ± 0.03 [21].

Unlike the case of the axial current matrix element, different flavors contribute differently to the DI of the scalar matrix element — s contributes less than u and d. As a result, the SU(3) antisymmetric and symmetric parameters $F_S=(\langle p|\bar{u}u|p\rangle-\langle N|\bar{s}s|N\rangle)/2$, $D_S=(\langle p|\bar{u}u|p\rangle-2\langle p|\bar{d}d|p\rangle+\langle N|\bar{s}s|N\rangle)/2$ are strongly affected by the large DI part. We see from Table II that both D_S and F_S compare favorably with the phenomenological values obtained from the SU(3) breaking pattern of the octet baryon masses with either linear [61,62] or quadratic mass relations [63]. This agreement is significantly improved from the valence quark model which predicts $F_S<1$ and $D_S=0$ and also those of the CI alone [61,62]. The latter yields $F_S=0.91(13)$ and $D_S=-0.28(10)$ which are only half of the phenomenological values [61–63]. This again underscores the importance of the sea quark contributions.

Next, we address the effect of the cloud quarks in the CI. Similar to the ratio R_A in the axial-vector case, we plot the ratio

$$R_S=\frac{g_S^{I=0}}{g_S^{I=1}}=\frac{\langle p|\bar{u}u+\bar{d}d|p\rangle}{\langle p|\bar{u}u-\bar{d}d|p\rangle} =\frac{(\langle p|\bar{u}u+\bar{d}d|p\rangle)(\mathrm{CI})+(\langle p|\bar{u}u+\bar{d}d|p\rangle)(\mathrm{DI})}{\langle p|\bar{u}u-\bar{d}d|p\rangle} \tag{83}$$

as a function of the quark mass in Fig. 12.

The dotted line is the valence quark model prediction of 3 for both the nonrelativistic and relativistic cases. Again for heavy quarks (i.e., $\kappa\geqslant 0.133$ or $ma\geqslant 0.4$ in Fig. 12), we see that the ratio R_S is 3 irrespective whether the DI is included (shown as ● in Fig. 12) or not (CI alone is indicated as ○). As for light quarks, the full result (CI+DI) is much larger than 3 largely due to the large sea contribution in the DI (Table II lists the results at the chiral limit). Even for the CI alone, R_S still overshoots 3. As we shall see, this is again caused by the cloud quarks. For VQCD, the R_S ratio becomes

$$R_S=\frac{(\langle p|\bar{u}u+\bar{d}d|p\rangle)(\mathrm{CI})}{(\langle p|\bar{u}u-\bar{d}d|p\rangle)(\mathrm{CI})}. \tag{84}$$

We see in Fig. 12 that the ratios (denoted by ◇) for the light quarks are approaching the valence quark prediction of 3. This again confirms that the deviation of the CI result in QCD is primarily due to Z graphs with cloud quarks and antiquarks. When they are eliminated in VQCD, R_S becomes close to the SU(6) relation.

The D_S/F_S ratio in VQCD is

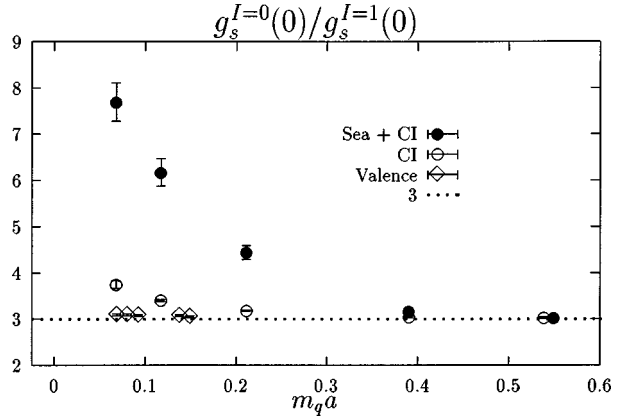

FIG. 12. The ratios R_S between isoscalar and isovector scalar charge in QCD [Eq. (83)] and VQCD [Eq. (84)] are plotted against the dimensionless quark mass $m_q a$ from the strange to the charm region. ○/● indicates CI/sea+CI in the QCD case and ◇ indicates the VQCD case. The dashed line is the valence quark model prediction of 3.

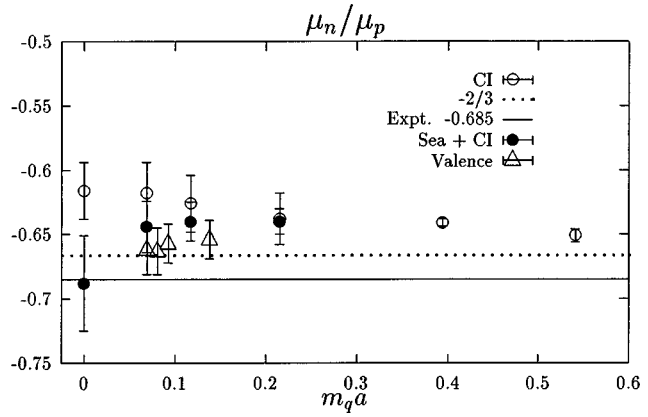

FIG. 13. The neutron to proton magnetic moment ratio μ_n/μ_p is plotted against the dimensionless quark mass. ○ indicates the CI result only and ● shows the full result with both CI and DI. △ indicates the ratio in the VQCD case. The solid line is the valence quark model prediction of $-2/3$ and the dashed line is the experimental result of -0.685.

$$D_S/F_S(\mathrm{CI}) = \frac{3-R_S}{1+R_S}. \tag{85}$$

From $R_S = 3.086(19)$ for the smallest quark mass ($\kappa = 0.162$), we obtain $D_S/F_S = -0.021(4)$ which is close to zero as in the valence quark picture (Table II) and differs from the lattice QCD calculation of $-0.58(18)$ (sea+CI) and $-0.31(11)$ (CI) (see Table II) by a large margin.

C. Neutron to proton magnetic moment ratio

After having established the importance of the sea and cloud effects in the axial and scalar matrix elements, one would naturally ask what happens to the vector current matrix elements, especially the neutron to proton magnetic moment ratio μ_n/μ_p. How much will the sea and cloud affect the ratio and in what way? After all, the μ_n/μ_p ratio was well predicted by the valence picture — a celebrated defining success of the SU(6) symmetry.

It has been known for some time that a nontrivial sea quark contribution to baryon magnetic moments is essential to reproducing the experimental moments [64–66]. It turns out that the individual sea contribution of each flavor is not small [66,47]. Although the central value of our lattice result [$G_M^s(0) = -0.36 \pm 0.20$ [47]] differs in sign from that of the SAMPLE experiment which has $G_M^s(Q^2 = 0.1\ \mathrm{GeV}^2) = +0.23 \pm 0.37 \pm 0.15 \pm 0.19$ from the elastic parity violating electron scattering [67], they are consistent within errors. The u and d contributions are $\sim 80\%$ larger, $G_M^{u,d}(0)(\mathrm{DI}) = -0.65 \pm 0.30$. However, their net contribution to the proton and neutron magnetic moments,

$$\mu(\mathrm{DI}) = [2/3 G_M^u(0)(\mathrm{DI}) - 1/3 G_M^d(0)(\mathrm{DI}) - 1/3 G_M^s(0)]\mu_N = -0.097 \pm 0.037 \mu_N, \tag{86}$$

becomes smaller due the cancellation of the quark charges of u, d, and s.

As illustrated in Fig. 13, where the neutron to proton magnetic moment ratio is plotted against the quark mass, this small SU(6) breaking sea quark effect is further nullified by the cloud effect [47]. As a result, the μ_n/μ_p ratio for the combined CI and DI comes to -0.68 ± 0.04 at the chiral limit. This is quite consistent with the experimental value of 0.685. Barring any as yet unknown symmetry principle, this cancellation between the cloud and sea contributions is probably accidental and in stark contrast to the $\pi N \sigma$ term and flavor-singlet g_A^0 where the cloud and sea effects add up to enhance the SU(6) breaking.

Also shown in Fig. 13 are results of VQCD (indicated as △) which are very close to the SU(6) value of $-2/3$ [the result for the smallest quark mass case is $-0.662(22)$], indirectly verifying the cloud effects of QCD (○ for the CI in Fig. 13) which shows a 2.5σ departure from $-2/3$ at the chiral limit. If there is any deviation of the VQCD from $-2/3$, it should be due to the residual spin-spin interaction between the quarks in the baryon. Given the size of the error in our present results, we cannot make a definite conclusion on this aspect.

VI. FORM FACTORS

In all the ratios we considered in the preceding section, i.e., R_A, R_S, and μ_n/μ_p, the SU(6) breaking due to the cloud in the Z graphs is at the level of 10 – 20 % which is relatively small compared with, say, the sea quark effect in R_S. However, its effect is large in the nucleon form factors and has been a subject of wide interest.

A. Meson dominance

The dipole form of the nucleon electromagnetic and axial form factors is interpreted as the product of two monopoles. For example, the isovector part of the nucleon Dirac form factor can be written as [68]

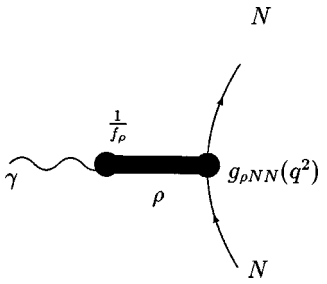

FIG. 14. The schematic diagram which depicts the photon coupling to the nucleon going through the ρ meson in a vector dominance picture.

$$F_1^V(q^2)=\frac{1}{2}[F_1^p(q^2)-F_1^n(q^2)]=\frac{1}{2}\,\frac{1}{1-q^2/m_\rho^2}\,\frac{g_{\rho NN}(q^2)}{f_\rho} \tag{87}$$

to reflect that the dominating process is the photon coupling to the ρ meson which in turn couples to the nucleon as shown in Fig. 14.

One monopole in $F_1^V(q^2)$ is the ρ meson propagator, and the other one is $g_{\rho NN}(q^2)=f_\rho(\Lambda^2-m_\rho^2)/(\Lambda^2-q^2)$ to parametrize the ρNN vertex (see Fig. 14). By the same token, the isovector axial form factor with axial meson dominance takes the form [69]

$$g_A^3(q^2)=\frac{g_A^3(0)}{1-q^2/m_{a_1}^2}\,g_{a_1NN}(q^2), \tag{88}$$

where $g_{a_1NN}(q^2)$ is the a_1NN vertex and can be parametrized with a monopole form. The isovector pseudoscalar form factor should reflect the pion pole for small q^2 and has the form

$$g_P^3(q^2)=\frac{g_P^3(0)}{1-q^2/m_\pi^2}\,\frac{g_{\pi NN}(q^2)}{g_{\pi NN}(0)}, \tag{89}$$

where $g_{\pi NN}(q^2)$ is the πNN form factor. Thus one of the major differences of the various form factors of the nucleon is reflected in the mass of the meson which dominates the matrix element in the t channel for the specific current. We plot in the following the isovector axial form factor $g_A^3(q^2)$, the proton electric form factor $G_E^p(q^2)$, the strangeness scalar form factor $g_S^s(q^2)$ [21], and the isovector pseudoscalar form factor $g_P^3(q^2)$ [20] in Fig. 15. We should mention in passing that both $G_E^p(q^2)$ and $g_A^3(q^2)$ shown in Fig. 15 from the lattice calculations [45,47] agree with the experiments within $\sim 6\%$.

We see that, since $g_A^3(q^2)$ and $g_P^3(q^2)$ involve only the CI and $G_E^p(q^2)$ is dominated by the CI [47], their different behaviors in q^2 reflect the ρ, a_1, and π propagators in the cloud which serve as the intermediate states in the meson dominance picture as depicted in Fig. 16.

If one assumes that $g_{\rho NN}(q^2)$, $g_{a_1NN}(q^2)$, and $g_{\pi NN}(q^2)$ have a similar form in q^2, then the fact that $g_P^3(q^2)$ falls off faster than $G_E^p(q^2)$ which in turn falls off faster than $g_A^3(q^2)$

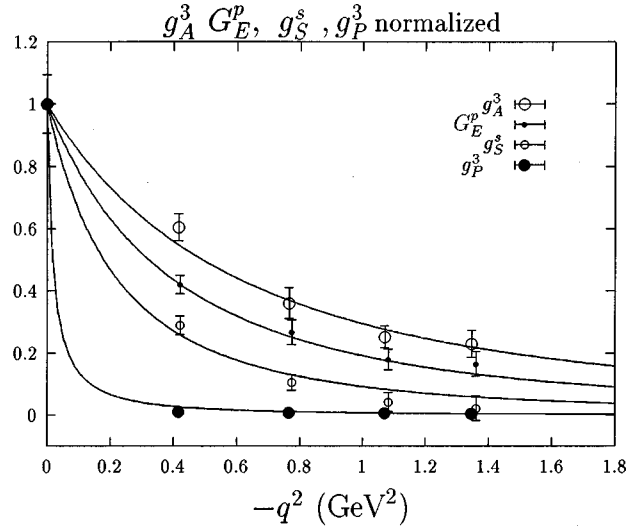

FIG. 15. The isovector axial form factor $g_A^3(q^2)$, the proton electric form factor $G_E^p(q^2)$, the strangeness scalar form factor $g_S^s(q^2)$, and the isovector pseudoscalar form factor $g_P^3(q^2)$ are plotted as a function of $-q^2$.

is to be expected, since experimentally $m_{a_1}=1230$ MeV $>m_\rho=769$ MeV$>m_\pi=140$ MeV. This is clearly a manifestation of the cloud quark effect through the meson cloud. We can attempt to define the meson-nucleon vertex by dividing the form factors in Eqs. (87), (88), and (89) by their respective meson propagators. These are plotted in Fig. 17. We see that the resulting $g_{\rho NN}(q^2)$, $g_{a_1NN}(q^2)$, and $g_{\pi NN}(q^2)$ extracted this way are much closer to each other than those in Fig. 15. We should mention that the monopole fit of $g_{\pi NN}(q^2)$ gives $g_{\pi NN}(0)=12.2\pm 2.3$ which confirms the Goldberger-Treiman relation [46].

Also plotted in Fig. 15 is the strangeness scalar form factor $g_S^s(q^2)$ which is from the DI [Fig. 3(c)]. It is very soft and has been interpreted as due to the $K\bar{K}$ intermediate states as depicted in Fig. 18(a) [21]. The DI with u or d quarks are even softer [21] and are consistent with the dispersion analysis of $\pi\pi$ intermediate states in chiral perturbation theory (χPT) [58]. This appears to be the source of the pion and kaon loops in χPT [59] which are responsible for the

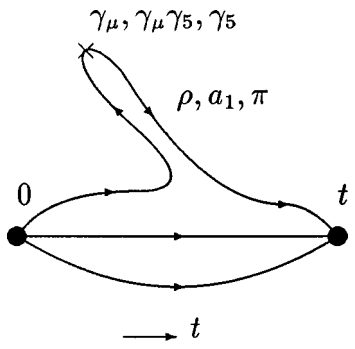

FIG. 16. The quark line diagram for the CI which illustrates the meson dominance picture with different intermediate meson state corresponding to the respective probing current.

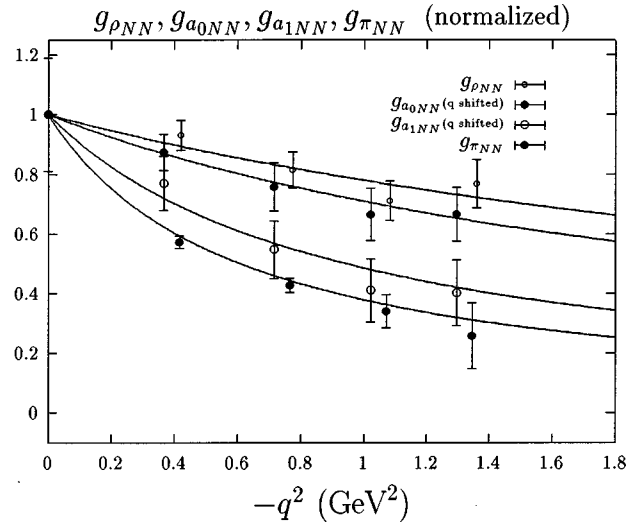

FIG. 17. The meson-nucleon-nucleon vertices $g_{\rho NN}(q^2)$, $g_{a_1 NN}(q^2)$, $g_{\pi NN}(q^2)$, and $g_{a_0 NN}(q^2)$ deduced from the EM form factors $g_A^3(q^2)$, $g_P^3(q^2)$ and the isovector scalar form factor $g_S^3(q^2)$ are plotted as a function of $-q^2$.

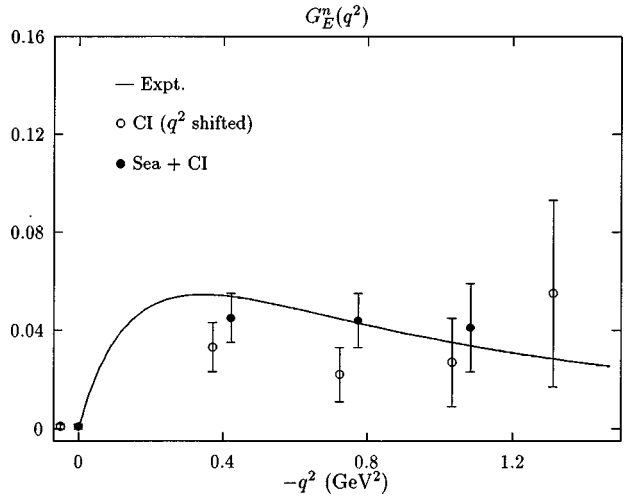

FIG. 19. The neutron electric form factor $G_E^n(q^2)$ together with the fit to the experimental result (solid line). The ○ indicates the CI contribution and the ● shows the full result with both the CI and the DI.

nonanalytic contribution of $m_q^{3/2}$ or m_π^3 and m_K^3 in hadron masses [see Fig. 18(b)]. This nonlinear dependence on the quark masses or m_π^2 has been observed prominently in hadron masses with dynamical fermions in lattice simulations [70]. This illustrates the sea quark effect in hadron masses and form factors. The neutron charge form factor in the strict SU(6) quark model would be identically zero, since the positively charged u quark and the negatively charged d quarks have the same spatial wave function. Thus, the small positive $G_E^n(q^2)$ signals the effects of the cloud and the sea without the contamination of the valence part like in other quantities. We present the lattice calculation of $G_E^n(q^2)$ [47] in Fig. 19 together with the experimental result. It is seen that both the cloud from the CI and the sea from the DI are positive and their contributions are similar in size.

B. Density and size of nucleon

Now, we can look at the time averaged radial density distribution of the nucleon due to different current probes. Define the time-averaged density distribution as

$$\rho(r) = N\frac{1}{(2\pi)^2}\int dt d^4q e^{i(\vec{q}\cdot\vec{r}-q_0 t)}F(q^2)$$

$$= N\frac{1}{(2\pi)^{3/2}}\int d^4q\,\delta(q_0)e^{i\vec{q}\cdot\vec{r}}F(q^2), \qquad (90)$$

where N is the normalization factor so that $\int d^3r\rho(r)=1$. We plot the pseudoscalar density $\rho_P(r)$, the scalar strangeness density $\rho_S^s(r)$, the electric charge density $\rho_c(r)$, and the axial current density $\rho_A(r)$ so obtained from $g_P^3(q^2)$, $g_S^s(q^2)$, $G_E^p(q^2)$, and $g_A^3(q^2)$ in Fig. 20.

We see that $\rho_P(r)$ has the longest range. This is presumably due to the pion cloud which dominates the pseudoscalar channel and has the longest Compton wavelength of all hadrons. The next longest is the scalar strangeness density $\rho_S^s(r)$ which seems to reflect the $K\bar{K}$ meson intermediate states in Fig. 18(a) and corresponds to the kaon loop in chiral perturbation theory as shown in Fig. 18(b). Then comes the electric charge density in the proton $\rho_c(r)$ which is well known and has been frequently used to extract the size of the nucleon. Finally, the one with the smallest size is the axial current density $\rho_A(r)$ which reflects the small Compton wavelength of the a_1 meson.

Now what is the size of the nucleon? As seen from Fig. 20, it is in the eyes of the beholder. In other words, it depends on what probe is used to measure it. It ranges from 3.56(3) fm for the pseudoscalar density, 1.06(9) fm for the strangeness density, and 0.797(29) fm for the proton charge density, to 0.627(29) fm for the axial current density, a large variation.

We see that even though the clouds in the CI do not break the SU(6) symmetry as much as the seas in the DI for the scalar and axial currents, they afford a large variation in hadron form factors and sizes. Short of these meson clouds, the valence quark model simply is not capable of delineating

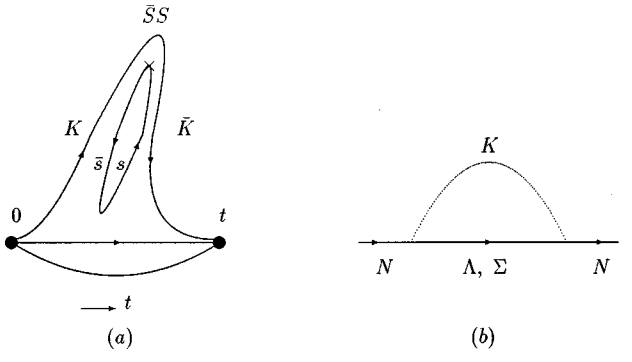

FIG. 18. (a) The quark line diagram which illustrates the $K\bar{K}$ intermediate states which dominates the form factor $g_S^s(q^2)$. (b) The kaon loop diagram in chiral perturbation theory.

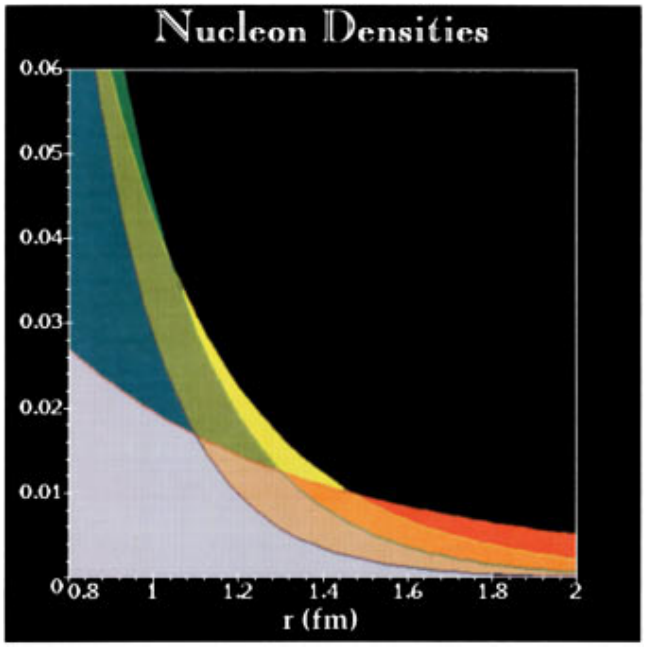

FIG. 20. (Color) The normalized pseudoscalar density $\rho_P(r)$ (in red), the scalar strangeness density $\rho_S^s(r)$ (in yellow), the electric charge density $\rho_c(r)$ (in green), and the axial current density $\rho_A(r)$ (in blue) are plotted as a function of the radial distance from the center of the nucleon.

the richness of the various form factors. A model like the Skyrmion, on the other hand, is capable of detailing the Goldberger-Treiman (GT) relation [28], the meson dominance of the nucleon form factors [68,71], negative square charge radius of the neutron [28], etc. All these are achieved via the ingredient of the meson clouds.

C. Form factors in VQCD

We calculated the isovector-axial form factor $g_A^3(q^2)$, the isoscalar-scalar form factor $g_S^0(q^2)$, the proton electric form factor $G_E^p(q^2)$, and the isovector pseudoscalar form factor $g_P^3(q^2)$ in VQCD at $\kappa=0.162$, which corresponds to the quark mass of $\sim$120 MeV. They are plotted in Fig. 21 as a function of $-q^2$. For comparison, we also plot in Fig. 22 the corresponding form factors from QCD at $\kappa=0.154$, which is about the same quark mass as in the VQCD case.

We see that although these form factors in VQCD are still different among themselves, the differences are relatively smaller compared to those in QCD first of all and, second, they are overall harder [except for $g_S^0(q^2)$]; i.e., they fall off slower than the corresponding ones in QCD. The most dramatic change is the pseudoscalar form factor where the size as determined by $\langle r^2\rangle=-6[dF(q^2)/d(-q^2)]|_{q^2=0}$ is reduced by about a factor of 2. This is consistent with the pseudoscalar meson-dominance picture in Fig. 16, where the pseudoscalar form factor in QCD is dominated by the pion which in turn couples to the baryon through the πNN vertex. Yet, this meson ''cloud'' is removed in VQCD by prohibiting pair creation. In this case, the current couples directly to

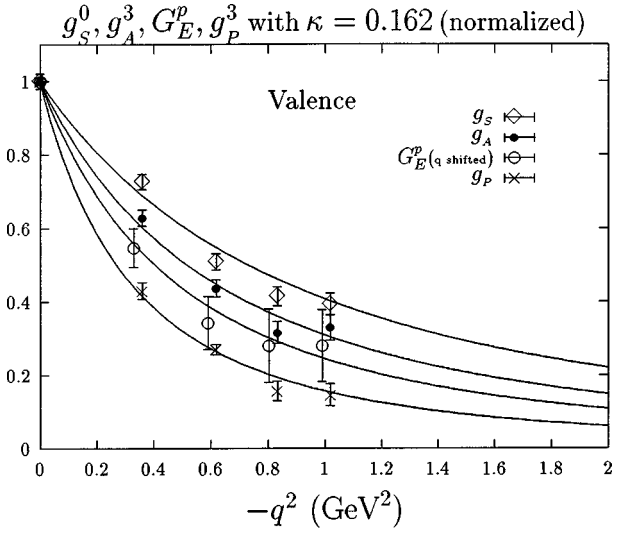

FIG. 21. The isovector axial form factor $g_A^3(q^2)$, the isoscalar scalar form factor $g_S^0(q^2)$, the proton electric form factor $G_E^p(q^2)$, and the isovector pseudoscalar form factor $g_P^3(q^2)$ in VQCD at $\kappa=0.162$ which corresponds to the quark mass of $\sim$120 MeV are plotted in terms of $-q^2$. They are normalized at $q^2=0$ to 1 in order to compare their q^2 dependence.

the quarks and consequently the $\langle r^2\rangle$ of the hadron becomes smaller. To a lesser extent, similar situations occur in the vector and axial channels. This is again an indirect way of visualizing the meson clouds effects in the CI.

We also plot the neutron electric form factor $G_E^n(q^2)$ for VQCD at $\kappa=0.162$ and its counterpart (CI QCD at $\kappa=0.154$) in Fig. 23. We see that these two results are comparable in size and indicate that there are still some spin-spin correlation between the quarks in VQCD which breaks the SU(6) symmetry.

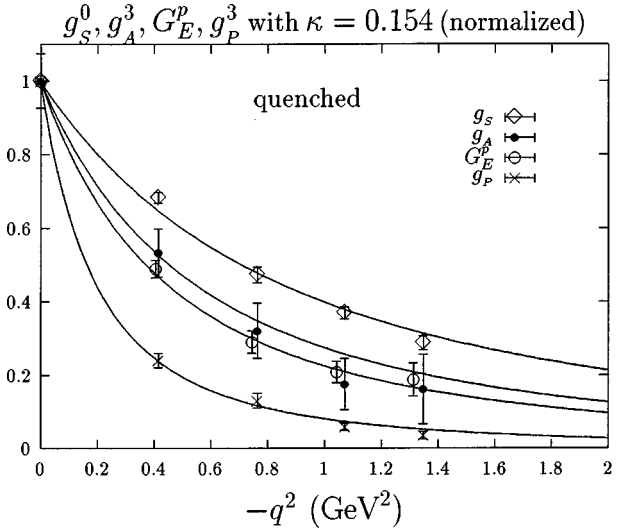

FIG. 22. For comparison, the same $g_A^3(q^2)$, $g_S^0(q^2)$, $G_E^p(q^2)$, and $g_P^3(q^2)$ in QCD at $\kappa=0.154$ which is at about the same quark mass, i.e., $\sim$120 MeV, are plotted in terms of $-q^2$. They are also normalized to 1 at $q^2=0$.

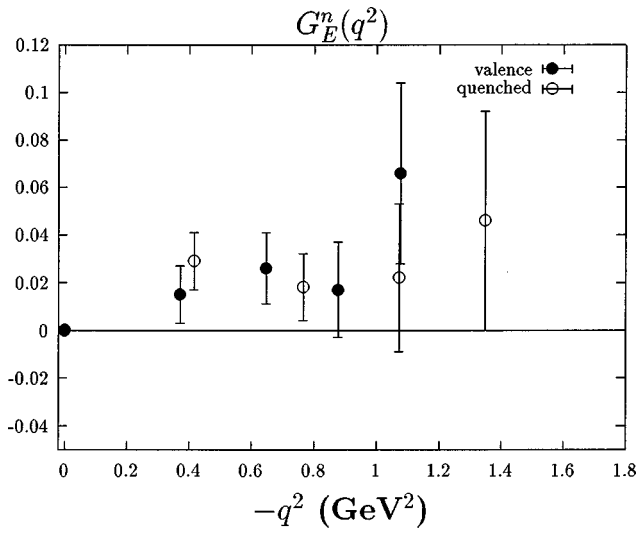

FIG. 23. The neutron electric form factor $G_E^n(q^2)$ for VQCD (●) at $\kappa=0.162$ is compared with the QCD result (○) at $\kappa=0.154$.

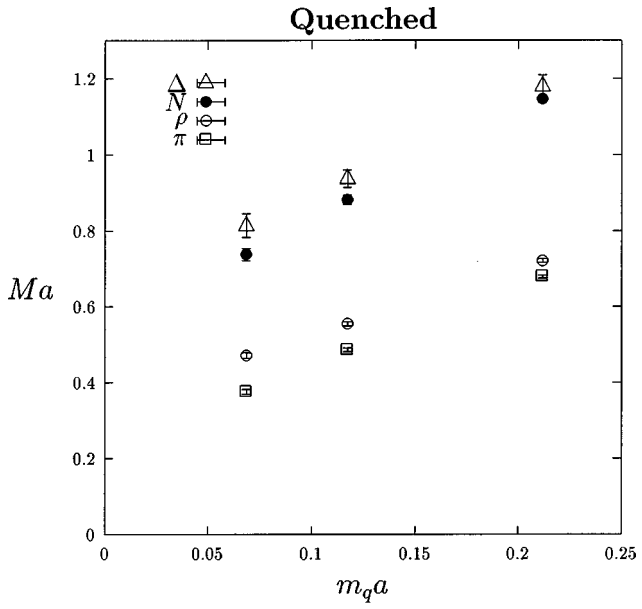

FIG. 24. The dimensionless Δ, N, ρ, and π masses in quenched QCD are plotted as a function of the quark mass $m_q a=\ln(4\kappa_c/\kappa-3)$. The pion mass is proportional to $\sqrt{m_q a}$, while the others are extrapolated to the chiral limit with a linear m dependence.

D. Goldberger-Treiman relation and vector dominance

There are several interesting aspects to observe in VQCD. Since the axial Ward identities in Eqs. (30) and (31) are associated with the current involving both the u and v fields, they are applicable only to meson states with the creation and annihilation of quark-antiquark pairs. Thus, the identities are useful in addressing the relation of the ''pion'' mass and decay constant with the quark mass as PCAC is in QCD. On the other hand, it does not apply to baryons where only the quarks are involved. For example, the pseudoscalar current matrix element between the nucleon states does not have the pion pole as evidenced in Fig. 21. Consequently, there is no Goldberger-Treiman relation in VQCD. Conversely, the conserved vector current in Eq. (24) between the baryons and meson states leads to separately conserved quark and antiquark numbers. This entails the three-point function calculation as illustrated in Fig. 10(a). Yet it does not apply to situations involving quark-antiquark creations or annihilations because the conserved vector current in Eq. (25) does not have the pair annihilation term $\bar{v}\gamma_\mu u$. Similarly, there is no vector dominance in the pion and nucleon EM form factors. As discussed in the preceding section, there should be no meson dominance in form factors in VQCD.

More generally, one can say that there is neither crossing symmetry, dispersion relation, nor unitarity in VQCD. But these features, or the lack of them, are shared by the valence quark model that we are trying to emulate.

VII. HADRON SPECTROSCOPY

To explore further the consequences of the valence approximation, we study the hadron masses. Since hadron masses entail calculations of two-point functions, the sea quarks do not appear explicitly as they do in three-point functions [see Fig. 10(b)]. The only exception is the flavor-singlet meson where the DI [Fig. 4(b)] is part of the meson propagator. The implicit sea quark effects in the loops which manifest themselves through the fermion determinant are known to affect the scaling [48], the topological susceptibility, phase transition, the η' mass, and the slope of the hadron mass with respect to the quark mass [21,70].

Here, we shall concentrate on the effects of the cloud quarks on hadron masses which are practically unknown. We first plot in Fig. 24 the masses of Δ, N, ρ, and π as a function of the quark mass $m_q a=\ln(4\kappa_c/\kappa-3)$ on our lattice with quenched approximation. We see that the hyperfine splittings between the Δ and N and the ρ and π grow when the quark mass approaches the chiral limit as expected.

In the infinite volume and continuum limits, it is found [49] that using m_ρ to set the scale, the K, Φ mesons and the octet and decuplet baryon masses are all within about 6% of the experimental results.

Next we plot in Fig. 25 the masses of Δ, N, ρ, and π from VQCD as a function of the quark mass $m_q a=\ln(4\kappa_c/\kappa-3)$ ($\kappa_c=0.1649$ in this case) on the same set of lattice configurations. It is a surprise that the truncation of the Z graphs appears to have such a dramatic effect on all these meson and baryon masses.

First of all, we notice that the Δ and the nucleon agree with each other within errors all the way down to the smallest quark mass around the strange quark range. Thus, the hyperfine splitting is largely gone in VQCD. This is true also between the ρ and π. Extrapolating to the zero-quark-mass limit, the ρ mass $m_\rho a$ is 0.054(8). With $a^{-1}=1.75$ GeV, $m_\rho=95(14)$ MeV in VQCD. This is a factor of 6.4 smaller than that in the quenched approximation which gives $m_\rho a=0.343(6)$. Second, we see that the masses of Δ, N, and ρ are all dropped greatly compared to those in QCD (Fig. 24). At the zero-quark-mass limit, $m_\Delta a=0.102(14)$, $m_N a=0.074(11)$. They are much smaller than their corresponding values of 0.638(41) and 0.536(13) in the quenched QCD

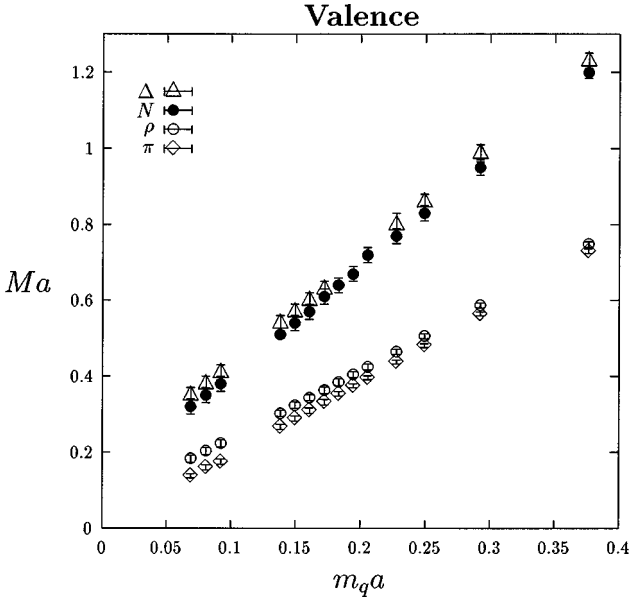

FIG. 25. The dimensionless Δ, N, ρ, and π masses in VQCD are plotted as a function of the quark mass $m_q a = \ln(4\kappa_c/\kappa - 3)$. All the masses are extrapolated to the zero-quark-mass limit with a linear m_q dependence.

calculation in Fig. 24. Furthermore, the hyperfine splitting between Δ and N is now 49(7) MeV which is ~ 3.7 times smaller than our quenched result of 179(11) MeV.[1]

For a more direct comparison to see how the nucleon and Δ masses drop, we plot the nucleon and Δ masses in VQCD and quenched QCD in Fig. 26. In going from quenched QCD to VQCD the nucleon mass is reduced by about a constant amount ~ 0.4 in lattice units or about 700 MeV. The Δ mass drops by the same amount for heavier quarks. For quarks around the strange, it drops further to meet the nucleon. We also plot the ρ and π masses in VQCD and quenched QCD in Fig. 27. Analogous to the N-Δ situation, the vector meson drops by about an equal amount ~ 0.31 or 537 MeV, whereas the pseudoscalar meson drops about 0.22 or 380 MeV in the strange region and approaches zero in both the quenched QCD and VQCD cases. Figures 26 and 27 show that at fixed quark mass VQCD leads to much smaller hadron masses than quenched QCD. It is quite revealing to ask how the quark mass in VQCD should be tuned in order to restore the hadron masses to realistic values. Using a lattice spacing $a^{-1} = 1.75$ GeV the results in Fig. 26 suggest a quark mass of about 300 MeV ($m_q a \sim 0.17$) is required. This is just in the range that quark models typically find for constituent masses.

Shown in Fig. 28 are the a_1 and a_0 mesons calculated in quenched QCD and VQCD. We see that both mesons come down in mass from QCD to VQCD by a large amount. a_1

[1]Our quenched result is smaller than the experimental Δ-N splitting of 298 MeV mainly due to the fact that our results are not in the infinite volume and continuum limits. It is shown that when these limits are taken, the octet and decuplet baryons are within 6% of the experimental values [49].

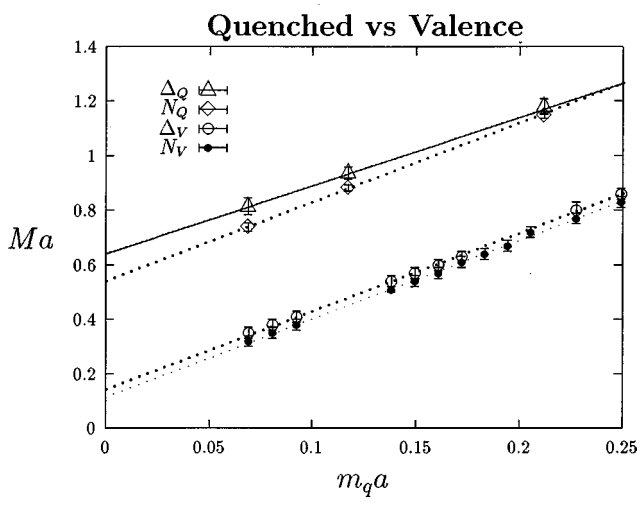

FIG. 26. The dimensionless N and Δ masses from QCD are compared with those in VQCD as a function of the quark mass.

appears to be degenerate with π and ρ in VQCD over the range of the quark mass in Fig. 27 and Fig. 25. However, we cannot be certain about this point, especially in view of the fact that the errors on a_1 for the three lightest quarks are quite large. a_0, on the other hand, seems to be heavier than the pion in this range of the quark mass.

A. Origin of hyperfine splitting

We see that the hyperfine splitting between Δ and nucleon has largely disappeared in the light quark sector when we remove the cloud quark and antiquark in the Z graphs. This is rather mysterious in that according to the usual lore, the hyperfine splitting is primarily due to the color-magnetic coupling induced spin-spin interaction between the quarks [6,17]. This color-magnetic coupling is related to the spatial motion of the quarks which should not be affected by the truncation of the Z graphs which only constrains the quark motion in the time direction. Indeed, this color-magnetic coupling is explicitly shown as $\vec{\sigma} \cdot \vec{B}$ in the Pauli spinor rep-

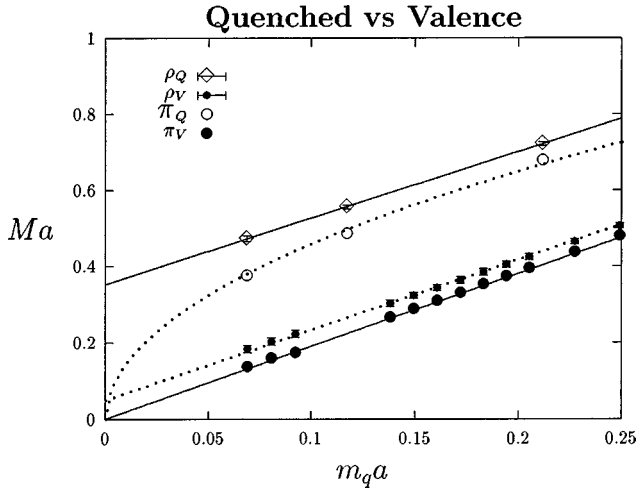

FIG. 27. The dimensionless π and ρ masses from QCD are compared with those in VQCD as a function of the quark mass.

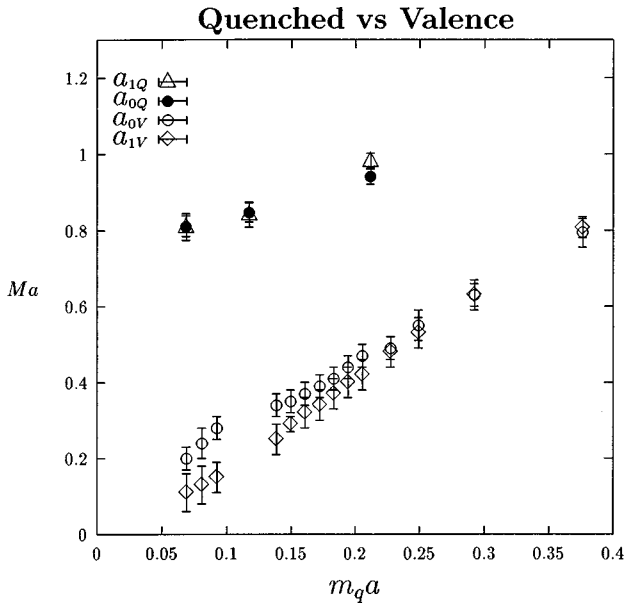

FIG. 28. The dimensionless a_1 and a_0 masses from QCD are compared with those in VQCD as a function of the quark mass.

resentation of VQCD in Eqs. (17) and (19). Furthermore, it is this $\vec{\sigma}\cdot\vec{B}$ term that is fully responsible for the hyperfine splitting between Υ and η_b in the heavy quark system. The latter is proved by the lattice QCD calculation with the nonrelativistic QCD action containing such a term in the form of $\vec{\sigma}\cdot\vec{B}/2M_b$ [3–5].

This raises a question as to how effective the color-spin interaction is as far as the hyperfine splitting is concerned in light hadron spectroscopy. The same question has been raised by Glozman and Riska [72,73]. Upon studying the negative parity and positive parity excitations of the N, Δ, and Λ spectra, they found that the reverse ordering of the positive and negative parity resonances of N and particularly Δ from those of the Λ cannot be accommodated with the color-spin structure of the pairwise interaction $\lambda_i^c\cdot\lambda_j^c\vec{\sigma}_i\cdot\vec{\sigma}_j$; instead it is consistent with the flavor-spin structure $\lambda_i^F\cdot\lambda_j^F\vec{\sigma}_i\cdot\vec{\sigma}_j$. This is so because flavor-spin structure of Λ is different from that of N and Δ. Interpreting this as due to Goldstone boson exchange, they can fit the low-lying baryon spectrum with a confinement potential in addition. They can also fit the magnetic moments of the baryon octets by taking into account of the meson exchange currents [73,74].

A similar problem was encountered in searching for scalar diquark clustering in lattice hadron form factors [75]. Significant scalar diquark clustering is predicted in quark models which rely on the hyperfine interaction of the one-gluon-exchange-potential (OGEP) to split the N and Δ. While significant mass splitting is seen in the lattice simulations of Refs. [75–77] there is no evidence of scalar diquark clustering. This result leads one to look for other sources of hyperfine splitting that do not necessarily lead to clustering in the wave function, such as meson exchange [75].

Furthermore, it is well known from the light baryon spectrum that the spin-orbit interaction is much weaker

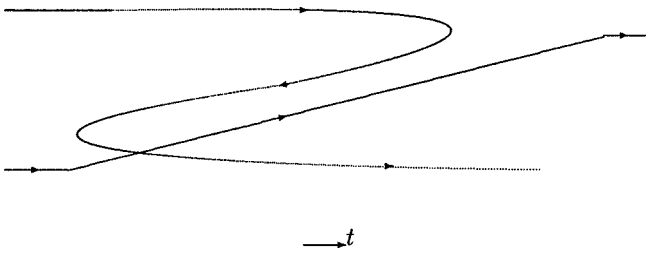

FIG. 29. The meson exchange between quarks in the baryon is depicted as a Z graph. The antiquark produced in the Z graph forms a meson with another quark in this case which is ''exchanged'' between the two quarks.

[78,79,9,10,8] than that which accompanies the spin-spin interaction in the one-gluon-exchange picture [6]. This is problematic for the gluon-exchange picture if it is to explain both heavy quarkonia which require a spin-orbit interaction and light baryons which require a much weaker one. However, Goldstone boson exchange does not have the spin-orbit interaction between the light quarks and, hence, has no problem in this regard.

This Goldstone-boson-exchange picture appears to be quite consistent with what we find in VQCD. The flavor-nonsinglet meson exchange between the quarks is represented by the Z graph depicted in Fig. 29. Since all the Z graphs are removed in VQCD, there will be no meson exchanges between the quarks as a result. This can explain why the hyperfine splitting between Δ and nucleon is greatly reduced in VQCD (Fig. 26). But this does not answer the question as to why the color-magnetic coupling induced spin-spin interaction is not as effective in light baryons as in heavy quarkonium. While we do not have strong evidence for it, we note that one aspect of the light quark may contribute to the difference. Unlike those of the heavy quarks, the propagator of the light quarks in the background gauge field can fluctuate into color-singlet meson clouds, leading to meson dominance in various form factors (see Fig. 16). The range of fluctuation depends on the Compton wavelength of the meson. The longest range is the pion cloud as evidenced in the softness of the pseudoscalar form factor of the nucleon (Figs. 15 and 20). By the same token, Goldstone boson exchange between the quarks in Fig. 29 can have a range commensurate with its Compton wavelength. On the other hand, the range of one-gluon exchange is limited since the gluon is confined. If the range of Goldstone boson exchange is longer than the gluon confinement scale, the hyperfine interaction from Goldstone boson exchange is likely to be more effective than that from the color-magnetic coupling. In other words, the light quarks in the baryon have larger separations than those between the quarks and antiquarks in heavy quarkonia. Together with the limited range of the confined gluons, this could be the reason for the diminished color-magnetic coupling in light baryons.

B. Origin of dynamical quark mass

Another significant feature of the VQCD spectroscopy in Figs. 25, 26, 27, and 28 is that all the hadron masses drop substantially from their counterparts in QCD (including pion

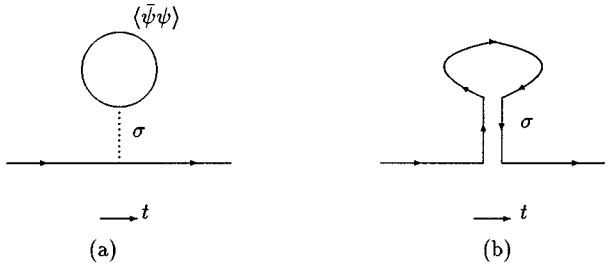

FIG. 30. (a) σ-quark tadpole diagram in the linear sigma model which is the mechanism for dynamical mass generation in this model. (b) The quark line diagram of the Z graph which corresponds to the σ-quark tadpole in (a).

at finite quark mass). For example, the nucleon moves down from 940 MeV in QCD (we used this to fix the scale) to 130(19) MeV in VQCD, Δ drops from 1117(72) MeV to 179(25) MeV, and ρ drops from 600(11) MeV to 95 (14) MeV. It is well known that chiral symmetry breaking leads to a dynamical quark mass related to the quark condensate [80], in addition to the existence of Goldstone bosons. This can be seen from

$$\langle\bar{\Psi}\Psi\rangle=\langle\bar{\Psi}_L\Psi_R+\bar{\Psi}_R\Psi_L\rangle, \tag{91}$$

which mixes the left- and right-handed quarks and has the effect of a dynamical mass as a result of the chiral symmetry breaking.

To the extent that we can interpret the falling hadron masses in VQCD as due to the drop of dynamical or constituent quark mass, we can draw the following conclusions.

(1) It is usually assumed in valence quark models that constituent quark mass arises due to dressing by the glue and the sea quark-antiquark pairs. Since the hard glue dressing in VQCD is expected to be the same as in QCD, it is not likely to be responsible for the dropping of hadron masses in VQCD. Furthermore, the quenched lattice calculations [49] can reproduce the ρ, K, Φ mesons and the octet and decuplet baryon masses to within about 6% of the experimental results. This is an indication that the quark loops which generate sea quark-antiquark pairs are not the primary source for hadron masses either. Here we see from our lattice calculation of VQCD that the dynamical quark mass actually arises from the ''dressing'' of the cloud quarks — quark-antiquark pairs in the connected insertion.

(2) In chiral symmetry models, the dynamical mass is generally generated through the σ — the chiral partner of the pion. For example, in the linear sigma model, the dynamical mass is given [81,82] as

$$m_{dyn}=\frac{g^2_{\sigma qq}}{-m^2_\sigma}\langle\bar{\Psi}\Psi\rangle_{m_\sigma}, \tag{92}$$

where m_σ and $g_{\sigma qq}$ are the σ mass and its coupling to the quark. This is represented as the σ-quark tadpole diagram illustrated in Fig. 30(a). A similar mechanism exists in the four-fermion Nambu–Jona-Lasinio model [83]. In QCD, the quark-line diagram which corresponds to the σ-quark tadpole in Fig. 30(a) would look something like Fig. 30(b) which inevitably involves cloud quarks and antiquarks in the Z graph.

This σ-quark tadpole interpretation is consistent with what we observe in VQCD. Dropping Z graphs in VQCD, which include these tadpoles, diminishes the coupling to the quark condensate $\langle\bar{\Psi}\Psi\rangle$ and leads to the falling of all the hadron masses from QCD. However, there is still a class of tadpole diagrams which survive. These are the spatial moving quark loops restricted within time slices. They may still couple to $\langle\bar{u}u\rangle$ and $\langle\bar{v}v\rangle$. But since these condensates in VQCD are much smaller than that in QCD, the dynamical mass is also much smaller. This can explain why the masses of Δ, N, and ρ are small but nonzero in VQCD (Figs. 25, 26, and 27).

The interpretation we offer for the hyperfine splitting and the dynamical quark mass is reminiscent of the little bag [84], the cloudy bag [85], and the chiral quark models [86] on which the phenomenological studies of baryon masses [72–74] and baryon structure [87,88] are based. Arguing that the chiral symmetry breaking scale $\Lambda_{\chi SB}$ is higher than the confinement scale Λ_{QCD}, it is proposed [86] that the relevant dynamical degrees of freedom are the fundamental quarks, gluons, and the Goldstone bosons in an effective theory at intermediate scales between $\Lambda_{\chi SB}$ and Λ_{QCD}. What we observe in VQCD seems to suggest that the scale for the structure of baryons falls just in this range so that the coupling to Goldstone bosons and dynamical mass generation are evident when QCD and VQCD are compared.

There are other suggestions for the flavor-spin structure of the quark-quark interaction. These are induced by instantons [89,90]. It is known that the instantons give rise to chiral symmetry breaking and generate dynamical quark mass associated with $\langle\bar{\Psi}\Psi\rangle$ [91,92]. The point-to-point hadronic correlation functions in the instanton liquid model [93] have been verified by lattice QCD calculation [94] and the role of instantons is revealed through cooling [95]. Although its direct connection to the cloud degree of freedom in relation to VQCD is less transparent, the instanton picture, being the root of chiral symmetry breaking, is expected to reproduce the consequences of the chiral quark model.

VIII. SYMMETRY BREAKING

It is well known that the chiral symmetry $\mathrm{SU}(N_F)_L\times\mathrm{SU}(N_F)_R\times\mathrm{U}_V(1)$ of QCD is spontaneously broken to the diagonal $\mathrm{SU}_V(N_f)\times\mathrm{U}_V(1)$. VQCD, as we have learned in this study, has a different symmetry breaking pattern. It starts out with the $\mathrm{U}(2N_F)$ symmetry (see Sec. III C) with vector and axial symmetries in the particle-antiparticle space. From our lattice simulation, we find that the pseudoscalar mesons corresponding to the interpolation fields $\bar{u}\gamma_5 v$ and $\bar{v}\gamma_5 u$ become massless at the zero-quark-mass limit, the pion decay constant f_π is nonzero (it may actually diverge as $1/m_\pi$), and the condensates $\langle\bar{u}u\rangle$ and $\langle\bar{v}v\rangle$ do not vanish. We take these as the evidence for spontaneous breaking of the axial symmetry in Eqs. (30) and (31). This then leads to $\mathrm{U}_q(N_F)\times\mathrm{U}_{\bar{q}}(N_F)$ symmetry, which is the vector symmetry for the

quarks and antiquarks separately. Again by virtue of the lattice simulation, we find that the SU(6) relation holds quite well for the g_A^0/g_A^3 (or F_A/D_A), g_S^3/g_S^0 (or D_S/F_S), and μ_n/μ_p ratios. Furthermore, N and Δ are nearly degenerate; so are ρ and π. All these indicate that, although the SU(6) breaking color-magnetic coupling is present in the VQCD action [Eqs. (17), (18), and (19)], its effects are small. As a result, VQCD has an approximate higher symmetry, i.e., $U_q(2N_F)\times U_{\bar{q}}(2N_F)$, where the ''2'' represents the spin subgroup SU(2). This $U_q(2N_F)\times U_{\bar{q}}(2N_F)$ is just the nonchiral $U(6)\times U(6)$ symmetry of Dashen and Gell-Mann [96] for $N_F=3$ with quarks and antiquarks in the $(\mathbf{6},\mathbf{1})$ and $(\mathbf{1},\overline{\mathbf{6}})$ representations respectively. It was proposed as a ''good'' symmetry for ''stationary (i.e., bound) and quasistationary (i.e., resonant) states of hadrons at rest.'' It is interesting to note that after stripping off the sea and cloud quarks from QCD, we find that the remaining VQCD possesses the same symmetry.

IX. CONCLUSION: ANALOGY TO SHELL MODEL AND MANY BODY THEORY

Instead of simulating QCD, we have mutilated it with the VQCD approximation. The valence QCD theory we have constructed does not respect Lorentz invariance. It also violates unitarity, the dispersion relation, and crossing symmetry. But these are the attributes shared by the valence quark model which we set out to understand and our purpose of this study is to sort out the roles the various dynamical quark degrees of freedom play in different observables. This is much like the study of the brain.[2] One tries to correlate the dysfunction of a certain part of the body with the damage of a specific part of the brain to infer its controlling mechanism.

After defining the valence, the cloud, and the sea quarks from the hadronic tensor in deep inelastic scattering, we have been able to follow these degrees of freedom to three-point and two-point functions which are relevant to the quark model at low energies. Upon eliminating the cloud quarks in the connected insertion with the help of the VQCD action and the sea quarks in the disconnected insertion with the quenched VQCD calculation, we find from the ratios of g_A^0/g_A^3, g_S^3/g_S^0, μ_n/μ_p and the masses of N, Δ, ρ, and π that there is an approximate SU(6) symmetry in VQCD which emerges from shaking off the ''dressing'' cloud and sea quark-antiquark pairs. Its symmetry breaking pattern is distinct from that of QCD. We summarize the symmetry breaking pattern of QCD and VQCD in the following chart:

$$\text{QCD:}\quad \mathrm{SU}(N_F)_L\times\mathrm{SU}(N_F)_R\times\mathrm{U}_V(1)\Rightarrow\mathrm{SU}_V(N_F)\times\mathrm{U}_V(1)$$

$$\text{VQCD:}\quad \mathrm{U}(2N_F)\Rightarrow\mathrm{U}_q(N_F)\times\mathrm{U}_{\bar{q}}(N_F)$$

$$\Rightarrow\approx\mathrm{U}_q(2N_F)\times\mathrm{U}_{\bar{q}}(2N_F).$$

We should point out that the $U_q(2N_F)\times U_{\bar{q}}(2N_F)$ symmetry due to the spin degeneracy is only approximately true. We see that the ratio g_A^0/g_A^3 in Fig. 11 is not exactly 3/5 and the neutron electric form factor $G_E^n(q^2)$ in Fig. 23 is not exactly zero. The degeneracies between Δ and N and between ρ and π are not perfect either. These indicate that there are still some color-magnetic coupling induced spin effects. Nevertheless, it is a fairly good symmetry. What we have demonstrated in this study is that QCD has this approximate symmetry in its valence approximation in the manner of VQCD action. To our best knowledge, this is the connection between QCD and the valence quark model.

The relation of the valence quark model and QCD actually is analogous to that between the shell model of nuclei and the many body theory. It is perhaps instructive to point out the parallel developments in the history of nuclear physics and hadron physics as far as the fermion dynamical degrees of freedom are concerned. We recall that the raison d'être of the shell model consists of the pattern of energy levels, the spin and parity quantum numbers of nuclei, and the Schmidt lines for the magnetic moments of nuclei. Similar reasons, e.g., the mass pattern of baryons and mesons, SU(3) flavor symmetry, and the magnetic moments of proton and neutron lent their support for the existence of the quark model. Later experiments and theoretical developments in many body theory pointed out the inadequacies of the shell model and ideas such as collectivity of the giant resonances [97], pairing through the induced phonon-exchange interaction [98], and core polarization for the magnetic moments, or the Arima-Horie effect [99] were introduced. These involve the particle-hole degrees of freedom in the disconnected insertion which are the core polarization effects beyond the shell model. With the advent of QCD as the fundamental theory of quarks and gluons, similar ideas are introduced. For example, the resolution of the U(1) anomaly in terms of the topological susceptibility in the large N_c analysis by Witten [19] and Veneziano [19] is the schematic model [97] approach to generating the η' mass by the collective coupling between quark loops. The concept of quark and gluon condensates is certainly related to pairing in the many body theory. A lack of appreciation for vacuum polarization due to the sea quarks for flavor-singlet observables in the quark model has led to the ''proton spin crisis'' [20,54] and the $\pi N\sigma$ term puzzle [57,58,21]. The importance of Z graphs for the density dependence was pointed out for the effective nucleon-nucleon interaction [100], and the higher-density effects in the relativistic mean-field theory are largely due to the Z graphs with sigma meson exchanges [101]. The importance of the cloud quarks in hadrons through the Z graphs is just beginning to be unraveled. The violation of the Gottfried sum rule leading to $\overline{u}(x)\neq\overline{v}(x)$ is shown to be due to the cloud antiquarks [35]. Furthermore, we have learned in the present study that the hyperfine splitting in baryons and the dynamical quark mass are related to the cloud degree of freedom, which are probably the most surprising results of VQCD.

The valence quark model, as we come to realize it today, is just like the shell model in nuclear physics. The U(6) $\times$U(6) symmetry which comes with the valence quark model as the defining characteristic is not as good a symme-

[2]We thank T. Cohen for this analogy.

try as one tends to believe. Even with the supplement of SU(6) breaking one-gluon exchange, it does not capture the richness of the cloud degrees of freedom in various form factors and matrix elements in the connected insertions. Moreover, the lack of sea degrees of freedom in the disconnected insertions is responsible for its overestimate of the flavor-singlet g_A^0 by a factor of ~ 3 as well as its underestimate of the $\pi N\sigma$ term by a factor $\sim 3-4$. What it lacks appears to be the spontaneously broken chiral symmetry of QCD. This is exemplified in hadron spectroscopy where we find that the hyperfine splitting between N and Δ and the dynamical quark mass are related to the cloud quarks in the Z graphs.

One lesson we learned in this study is that the valence quark model is not necessarily a bad place to start building an effective theory of hadrons, provided one knows how to incorporate chiral symmetry and restores the cloud and sea degrees of freedom. Working in the intermediate scale between chiral symmetry breaking and confinement which is appropriate for studying hadron structure and spectroscopy, one may start with the chiral quark model [86]. Integrating out the short-range part of the quark field is shown to lead to a very successful effective chiral theory of mesons [102]. One may extend this to the baryon sector with the quark coupling to the gluons and mesons [84–86]. In this way, the cloud degrees of freedom will show up in the form factors and matrix elements via meson dominance and meson exchange currents. It can also give rise to hyperfine splitting and dynamical quark mass. The meson loops on the quark lines, on the other hand, are responsible for the sea degrees of freedom. We will study this effective theory of baryons in the future.

ACKNOWLEDGMENTS

This work is partially supported by U.S. DOE grant No. DE-FG05-84ER40154 and NSF Grant No. 9722073. The authors would like to thank T. Barnes, C. Bernard, S. Brodsky, G. E. Brown, T. P. Cheng, T. Cohen, M. Golterman, L. Ya. Glozman, X. Ji, J.-F. Lagaë, C. S. Lam, B. A. Li, R. McKeown, J. Negele, M. Rho, D. O. Riska, C. Roberts, J. Rosner, E. Shuryak, A. Thomas, W. Weise, U.-J. Wiese, and A. Williams for very useful discussions.

[1] See, for example, F. E. Close, *An Introduction to Quarks and Partons* (Academic, New York, 1979).
[2] J. Sloan, Nucl. Phys. B (Proc. Suppl.) **42**, 171 (1995).
[3] J. Shigemitsu, Nucl. Phys. B (Proc. Suppl.) **53**, 16 (1997).
[4] SESAM Collaboration, N. Eicker *et al.*, Nucl. Phys. B (Proc. Suppl.) **63**, 317 (1998).
[5] NRQCD Collaboration, C. T. H. Davies *et al.*, Nucl. Phys. B (Proc. Suppl.) **63**, 320 (1998); Phys. Rev. D **58**, 054505 (1998).
[6] A. De Rújula, H. Georgi, and S. L. Glashow, Phys. Rev. D **12**, 147 (1975).
[7] K. F. Liu and C. W. Wong, Phys. Rev. D **17**, 2350 (1978); **21**, 1350 (1980).
[8] K. F. Liu and C. W. Wong, Phys. Rev. D **28**, 170 (1983).
[9] N. Isgur and G. Karl, Phys. Rev. D **18**, 4187 (1978).
[10] N. Isgur and G. Karl, Phys. Rev. D **19**, 2653 (1979).
[11] L. Brekke and J. Rosner, Comments Nucl. Part. Phys. **18**, 83 (1988).
[12] L. G. Pondrom, Phys. Rev. D **53**, 5322 (1996).
[13] S. Ono, Nucl. Phys. **B107**, 522 (1976).
[14] R. Koniuk and N. Isgur, Phys. Rev. D **21**, 1868 (1980).
[15] J. F. Donoghue, E. Golowich, and B. R. Holstein, *Dynamics of the Standard Model* (Cambridge University Press, Cambridge, England, 1992).
[16] S. Okubo, Phys. Lett. **5**, 165 (1963).
[17] A. Chodos, R. L. Jaffe, K. Johnson, C. B. Thron, and V. F. Weisskopf, Phys. Rev. D **9**, 3471 (1974); A. Chodos, R. L. Jaffe, K. Johnson, and C. B. Thron, *ibid.* **10**, 2599 (1974).
[18] J. Donoghue and B. Holstein, Phys. Rev. D **29**, 489 (1984).
[19] E. Witten, Nucl. Phys. **B149**, 285 (1979); G. Veneziano, *ibid.* **B159**, 213 (1979).
[20] S. J. Dong, J.-F. Lagaë, and K. F. Liu, Phys. Rev. Lett. **75**, 2096 (1995).
[21] S. J. Dong, J.-F. Lagaë, and K. F. Liu, Phys. Rev. D **54**, 5496 (1996).
[22] S. Weinberg, Phys. Rev. Lett. **17**, 616 (1966).
[23] J. Gasser and H. Leutwyler, Nucl. Phys. **B250**, 465 (1985); **B250**, 517 (1985); **B250**, 539 (1985).
[24] J. J. Sakurai, Phys. Rev. Lett. **17**, 1021 (1966); *Currents and Mesons* (The University of Chicago Press, Chicago, 1969).
[25] K. Kawarabayashi and M. Suzuki, Phys. Rev. Lett. **16**, 255 (1966); Fayyazuddin and Riazuddin, Phys. Rev. **147**, 1071 (1966).
[26] Y. Tomozawa, Nuovo Cimento A **46**, 707 (1966).
[27] M. Mattis, in *Chiral Solitons*, edited by K. F. Liu (World Scientific, Singapore, 1987), p. 171.
[28] G. Adkins, C. R. Nappi, and E. Witten, Nucl. Phys. **B228**, 552 (1983).
[29] B. A. Li and K. F. Liu, in *Chiral Solitons* [27], p. 421.
[30] M. Goldberger and S. B. Treiman, Phys. Rev. **110**, 1178 (1958).
[31] G. 't Hooft, Nucl. Phys. **B72**, 461 (1974).
[32] E. Witten, Nucl. Phys. **B160**, 57 (1979).
[33] For a review, see, for example, *Chiral Solitons* [27].
[34] R. Dashen, E. Jenkins, and A. Manohar, Phys. Rev. D **49**, 4713 (1994).
[35] K. F. Liu and S. J. Dong, Phys. Rev. Lett. **72**, 1790 (1994).
[36] W. Wilcox, Nucl. Phys. B (Proc. Suppl.) **30**, 491 (1993).
[37] K. F. Liu (in preparation).
[38] E. Eichten and F. Feinberg, Phys. Rev. D **23**, 2724 (1981).
[39] S. Adler, Phys. Rev. **177**, 2426 (1969); J. Bell and R. Jackiw, Nuovo Cimento A **60**, 47 (1969).
[40] We thank M. Golterman for pointing this out to us.
[41] G. P. Lepage and P. B. Mackenzie, Phys. Rev. D **48**, 2250 (1993).

[42] K. Osterwalder and R. Schrader, Commun. Math. Phys. **31**, 83 (1973); **42**, 281 (1975); K. Osterwalder and E. Seiler, Ann. Phys. (N.Y.) **110**, 440 (1978).
[43] I. Montvay and G. Münster, *Quantum Fields on a Lattice* (Cambridge University Press, Cambridge, England, 1994), p. 182.
[44] M. Gell-Mann, R. Oakes, and B. Renner, Phys. Rev. **175**, 2195 (1968).
[45] K. F. Liu, S. J. Dong, T. Draper, J. M. Wu, and W. Wilcox, Phys. Rev. D **49**, 4755 (1994).
[46] K. F. Liu, S. J. Dong, T. Draper, and W. Wilcox, Phys. Rev. Lett. **74**, 2172 (1995).
[47] S. J. Dong, K. F. Liu, and A. G. Williams, Phys. Rev. D **58**, 074504 (1998).
[48] J. Sexton and D. Weingarten, Phys. Rev. D **55**, 4025 (1997).
[49] F. Butler, H. Chen, J. Sexton, A. Vaccarino, and D. Weingarten, Phys. Rev. Lett. **70**, 2849 (1993); Nucl. Phys. **B430**, 179 (1994).
[50] P. Maris and C. D. Roberts, in *Progress in Heavy Quark Physics*, Proceedings to the Workshop, Rostock, Germany, 1997, edited by M. Beyer, T. Mannel, and H. Schröder (University of Rostock, Rostock, 1998), nucl-th/9710062.
[51] EMC Collaboration, J. Ashman *et al.*, Phys. Lett. B **206**, 364 (1988).
[52] E143 Collaboration, K. Abe *et al.*, Phys. Rev. Lett. **74**, 346 (1995).
[53] SMC Collaboration, D. Adams *et al.*, Phys. Rev. D **56**, 5330 (1997).
[54] For a review, see H. Y. Cheng, Int. J. Mod. Phys. A **11**, 5109 (1996).
[55] M. Fukugita, Y. Kuramashi, M. Okawa, and A. Ukawa, Phys. Rev. Lett. **75**, 2092 (1995).
[56] F. E. Close and R. G. Roberts, Phys. Lett. B **316**, 165 (1993).
[57] T. P. Cheng, Phys. Rev. D **13**, 2161 (1976); **38**, 2869 (1988).
[58] J. Gasser, H. Leutwyler, and M. E. Sanio, Phys. Lett. B **253**, 252 (1991); **253**, 260 (1991).
[59] J. Gasser and H. Leutwyler, Phys. Rep. **87**, 77 (1982); J. F. Donoghue and C. R. Nappi, Phys. Lett. **168B**, 105 (1986).
[60] M. Fukugita, Y. Kuramashi, M. Okawa, and A. Ukawa, Phys. Rev. D **51**, 5319 (1995).
[61] L. Maiani *et al.*, Nucl. Phys. **B293**, 420 (1987).
[62] M. Okawa, Nucl. Phys. B (Proc. Suppl.) **47**, 160 (1996).
[63] J. Gasser, Ann. Phys. (N.Y.) **136**, 62 (1981).
[64] D. B. Leinweber, Phys. Rev. D **45**, 252 (1992).
[65] D. B. Leinweber, Nucl. Phys. **A585**, 341 (1995).
[66] D. B. Leinweber, Phys. Rev. D **53**, 5115 (1996).
[67] SAMPLE Collaboration, B. Mueller *et al.*, Phys. Rev. Lett. **78**, 3824 (1997).
[68] G. E. Brown, M. Rho, and W. Weise, Nucl. Phys. **A454**, 669 (1986).
[69] M. Gari and U. Kaulfuss, Phys. Lett. **138B**, 29 (1984).
[70] S. Collins, R. G. Edwards, U. M. Heller, and J. Sloan, Nucl. Phys. B (Proc. Suppl.) **47**, 378 (1996).
[71] U. G. Meissner, N. Kaiser, and W. Weise, Nucl. Phys. **A466**, 685 (1987).
[72] L. Ya. Glozman and D. O. Riska, π N Newslett. **10**, 115 (1995).
[73] L. Ya. Glozman and D. O. Riska, Phys. Rep. **268**, 263 (1996).
[74] L. Ya. Glozman, Z. Papp, and W. Plessas, Phys. Lett. B **381**, 311 (1996).
[75] D. B. Leinweber, Phys. Rev. D **47**, 5096 (1993).
[76] D. B. Leinweber, T. Draper, and R. M. Woloshyn, Phys. Rev. D **46**, 3067 (1992).
[77] D. B. Leinweber, R. M. Woloshyn, and T. Draper, Phys. Rev. D **43**, 1659 (1991).
[78] H. Dalitz, Prog. Part. Nucl. Phys. **8**, 7 (1982).
[79] D. Gromes and I. O. Stamatescu, Nucl. Phys. **B112**, 213 (1976).
[80] Y. Nambu and G. Jona-Lasinio, Phys. Rev. **122**, 345 (1961).
[81] V. Elias and M. D. Scadron, Phys. Rev. Lett. **53**, 1129 (1984).
[82] L. R. Baboukhadia, V. Elias, and M. D. Scadron, J. Phys. G **23**, 1065 (1997).
[83] C. V. Christov *et al.*, Prog. Part. Nucl. Phys. **37**, 1 (1996).
[84] G. E. Brown and M. Rho, Phys. Lett. **82B**, 177 (1979).
[85] A. W. Thomas, S. Theberge, and G. A. Miller, Phys. Rev. D **24**, 216 (1981).
[86] A. Manohar and H. Georgi, Nucl. Phys. **B234**, 189 (1984).
[87] A. W. Thomas, Adv. Nucl. Phys. **13**, 1 (1984).
[88] T. P. Cheng and L. F. Li, Phys. Rev. Lett. **80**, 2789 (1998); **74**, 2872 (1995).
[89] E. V. Shuryak and J. L. Rosner, Phys. Lett. B **218**, 72 (1989).
[90] G. 't Hooft, Phys. Rev. D **14**, 3432 (1976).
[91] T. Schäfer and E. V. Shuryak, Rev. Mod. Phys. **70**, 323 (1998).
[92] D. I. Diakonov and V. Yu. Petrov, Phys. Lett. **147B**, 351 (1984).
[93] E. V. Shuryak, Rev. Mod. Phys. **65**, 1 (1993).
[94] M. C. Chu, J. M. Grandy, S. Huang, and J. W. Negele, Phys. Rev. Lett. **70**, 255 (1993); Phys. Rev. D **48**, 3340 (1993).
[95] M. C. Chu, J. M. Grandy, S. Huang, and J. W. Negele, Phys. Rev. D **49**, 6039 (1994).
[96] R. F. Dashen and M. Gell-Mann, Phys. Lett. **17**, 142 (1965).
[97] G. E. Brown and M. Bolsterli, Phys. Rev. Lett. **3**, 472 (1959).
[98] T. T. S. Kuo and G. E. Brown, Nucl. Phys. **85**, 40 (1966).
[99] A. Arima and H. Horie, Prog. Theor. Phys. **11**, 509 (1954).
[100] G. Bertsch and T. T. S. Kuo, Nucl. Phys. **112**, 204 (1968).
[101] G. E. Brown, W. Weise, G. Baym, and J. Speth, Comments Nucl. Part. Phys. **17**, 39 (1987).
[102] B. A. Li, Phys. Rev. D **52**, 5165 (1995); **52**, 5184 (1995).